International Journal of Pharmaceutics 376 (2009) 22–40

Contents lists available at ScienceDirect

International Journal of Pharmaceutics

journal homepage: www.elsevier.com/locate/ijpharm

# Mathematical modeling of the fluid dynamics in the flow-through cell

Maziar Kakhi*

*Food and Drug Administration, Division of Pharmaceutical Analysis, Building 22, Rm 2147, 10903 New Hampshire Avenue, Silver Spring, MD 20993, USA*

ARTICLE INFO

*Article history:*
Received 22 December 2008
Received in revised form 3 April 2009
Accepted 6 April 2009
Available online 16 April 2009

*Keywords:*
Dissolution
Flow-through cell (USP 4)
Computational fluid dynamics (CFD)
Flow separation
Velocity boundary layer
Adverse pressure gradient
Open/packed column modes

ABSTRACT

The fluid dynamics in the flow-through cell (USP apparatus 4) has been predicted using the mathematical modeling approach of computational fluid dynamics (CFD). The degree to which flow structures in this apparatus can be qualified as 'ideal' both spatially and temporally has been assessed. The simulations predict the development of the velocity field in this apparatus for configurations with and without beads during the discharge stroke of the pump. When the cell is operated only with the red ruby bead ('open column' mode), highly non-uniform flow is predicted just downstream of the bead in the latter stages of the pump's pulse. In contrast, a strong degree of profile uniformity and symmetry is predicted throughout the entire pulse in the region of the tablet holder for both standard configurations involving beads. However, noticeable differences in the tablet shear stress distribution are predicted at times when the same instantaneous inlet flow rates are being pumped through the apparatus. This effect is caused by flow separation in the velocity boundary layer formed around the tablet under the influence of an adverse pressure gradient, an effect not predicted with constant (non-pulsating) flow. While the degree of tablet erosion correlates with the average flow rate, during a particular pulse both the free-stream velocity and the boundary layer thickness are also influential.

Published by Elsevier B.V.

## 1. Introduction

The dissolution test is a surrogate method for assessing a pharmaceutical dosage form's suitability for use. In the initial stages of formulation development dissolution testing is used to help identify the optimal balance of raw materials and processing parameters for achieving a targeted drug release rate. In combination with pharmacokinetic studies, *in vivo–in vitro* correlations (IVIVC) can be developed which link the drug release rate during the surrogate test to the absorption of the active ingredient in the patient's bloodstream. As a quality assurance test, dissolution testing is routinely performed to characterize dosage form variability resulting from fluctuations in raw materials and drift in manufacturing processing parameters.

Regardless of the working group's primary focus (formulation development, IVIVC or quality assurance), objectives cannot be addressed adequately if the *in vitro* dissolution test is incapable of generating accurate and reproducible data. Variability extrinsic to the true release rate behaviour of the dosage form under test can arise due to a range of factors such as vessel geometry, mechanical set-up, mixing rate and operating procedure. Dissolution testing presents a dichotomy in that a simple and easy-to-use apparatus is sought to achieve goals whose underlying science is fraught with complexity. Dissolution is a multivariable and multi-physics phenomenon and the myriad of dosage forms composed of raw materials with wide-ranging physico-chemical properties makes this field even more challenging. Dissolution testing is very often applied far downstream of a manufacturing supply chain, in which each stage can involve procedures which ultimately influence the result of the test. For example, a certain batch of tablets may have been subjected to higher compression in the tablet press, and a higher concentration of disintegrant during granulation. These effects could cancel each other out in terms of the dissolution profile so that no net change is noticeable. In this regard the test really serves more as a helpful guide rather than providing detailed diagnostics of the 'process signature'.

Dissolution science can be better understood using mathematical modeling tools which are routinely employed in other branches of engineering. One such tool is computational fluid dynamics (CFD), which has been successfully employed to provide more detailed insight into existing concepts which traditionally have been formed from empirical observations. In the basket apparatus (United States Pharmacopeia, 2008) (USP 1) CFD simulations indicate flow patterns that enter axially at the base of the basket, flow upwards and exit at its sides (D'Arcy et al., 2006). Furthermore, the same study shows that since the flow agitation from the rotating basket is very limited, natural convection plays an important role as a dominant transport process at the base of the basket dissolution vessel. Simulations of fluid flows in the paddle apparatus (USP 2) predict a three-dimensional flow field with a

* Tel.: +1 301 796 0082; fax: +1 301 796 9859.
*E-mail address:* Maziar.Kakhi@fda.hhs.gov.

0378-5173/$ – see front matter. Published by Elsevier B.V.
doi:10.1016/j.ijpharm.2009.04.012

low-velocity domain undergoing solid body rotation (McCarthy et al., 2003, 2004) directly below the center of the rotating paddle. This corresponds to the location of the dosage form where in the case of disintegrating tablets 'coning' takes place. The validity of the predictions from such simulations has been demonstrated by comparison with non-intrusive measurements (Bocanegra et al., 1990; Bai et al., 2007a), visualization of the velocity field (Kukura et al., 2003) and experimental blend times (Bai et al., 2007b). In the latter case, it has been shown that blend times at 50 rpm are typically less than 34 s. Based on this observation it is concluded that for dissolution kinetics, which is rate-limited by mass transfer from the solid into the solution phase, the liquid contents of the paddle apparatus can be considered relatively well mixed so that variability associated with the location of the sampling point should be insignificant. The lack of spatial homogeneity associated with 'beaker' methods has been one reason for the advent of designs with a smaller hold-up volume ensuring homogeneous conditions at mixing rates low enough to discriminate formulation differences in tablets (Tingstad and Riegelman, 1970). But the aforementioned result regarding blend time holds true once the drug is in solution. If solid, undissolved agglomerates float to the surface, where macroscale mixing is very poor, variable results can still be obtained in spite of the short blend times.

Based on the inhomogeneous distribution of velocity in the paddle apparatus, it has been demonstrated how small changes in tablet location can influence the dissolution rate (Kukura et al., 2004; Baxter et al., 2005; D'Arcy et al., 2005; Bai and Armenante, 2008). Since tablets are often dropped into the dissolution vessel at the start of testing, the likelihood of variable tablet locations is high (Bai et al., 2007a). It has been conjectured that much of the variability witnessed in dissolution testing for the paddle apparatus might be attributable to the inhomogeneity of the flow field (Kukura et al., 2004; Baxter et al., 2005). At the agitation rates typically occurring in this device, the impeller Reynolds number is of the order of $10^3$–$10^4$, indicating a flow that is no longer laminar (Tatterson, 1991). Consequently it has been suggested that the unsteadiness associated with turbulence may be the cause of observed inconsistencies in dissolution results (Kukura et al., 2003). However, it is known that high levels of agitation, which generate greater turbulent intensity, only serve to reduce variability (Hamlin et al., 1962), not increase it. Gauge repeatability and reproducibility studies of prednisone (NCDA #2) tablets demonstrate that 70% of the total observed variance is due to sample tablets, 25% from the apparatus and approximately 5% due to operators (Gao et al., 2007), suggesting that while flow effects are important, they are by no means the primary factor influencing variability.

The aim of this paper is to examine the flow structures in the flow-through cell (USP 4). This work builds on a previous study (Kakhi, 2009) which examines in some detail the flow regimes occurring in this device. The flow-through cell is claimed to possess "ideal hydrodynamic conditions for mild agitation, homogeneity and mathematically definable solvent flow pattern" (FIP, 1981). Its very proposal was, in part, motivated by the limitations of other methods (Möller, 1983). The present computational study attempts to verify some of these assertions. In particular, the degree of spatial uniformity of the flow and the effect of pulsations is of particular interest. The vessel chosen for this study is the 22.6 mm diameter (⌀22.6 mm) cell used for tablet dissolution, as illustrated in Fig. 1. In this work the conventionally cited operational modes, namely 'laminar' and 'turbulent', are referred to as 'packed column' and 'open column' (respectively) for reasons elaborated in a separate article (Kakhi, 2009).

The scientific literature associated with the flow-through cell highlights a number of flow-related interactions. In studies with disintegrating tablets, variability of test results in the flow-through cell was observed because of the lingering presence of undissolved tablet residues (Wennergren et al., 1989). As a consequence it was suggested that the paddle apparatus gives a more even disintegration of tablets at the stirring rates investigated. The rigorous basis for this assertion is not readily obvious. In another example, insufficient wetting of micronized powders led to their deposition on the filter resulting in less dissolution compared to un-micronized powders (Bhattachar et al., 2002). Tests performed with salicylic acid 'calibrator' tablets in the ⌀22.6 mm cell demonstrated no signifi-

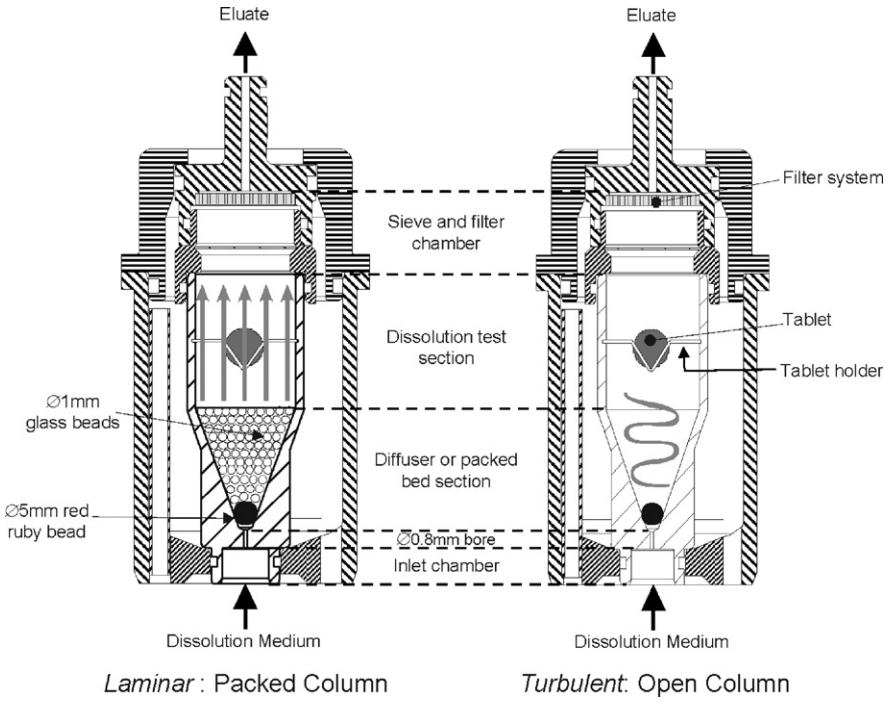


**Fig. 1.** Schematic of flow-through cell showing packed and open column configurations. (Reproduced with permission of SOTAX Corporation, 411 Caredean Dr Suite A, Horsham, PA 19044-1316, USA.)

cant difference in the dissolution rate below 51.2 ml/min (Cammarn and Sakr, 2000), the highest rate of delivery with the older CY 7-50 pump. An explanation for this observation might be that as the average column velocity drops, the time scales associated with mixing and mass transfer become comparable. Problems associated with local saturation at low flow rates have been alluded to in the past (Tingstad and Riegelman, 1970).

## 2. Development of simulation model

### 2.1. Computational methodology

Fluent (Ansys Inc., 2008), a commercial CFD package, is used to analyze the fluid dynamics in the flow-through cell. CFD solvers numerically integrate the conservations equations of fluid motion, expressed analytically as a coupled set of non-linear partial differential equations for mass, momentum and energy. In this work the energy equation is not considered because conditions in the flow are assumed isothermal, in other words it is assumed that the water jacket surrounding the dissolution cell is in thermal equilibrium with the dissolution medium. Furthermore, mass transfer from the solid oral dosage form into solution and its subsequent transport are not considered; only the flow in the dissolution apparatus is being studied.

The concept of the control volume is at the core of most analyses in fluid mechanics. The control volume (schematically illustrated in Fig. 2) represents, in the mathematical limit, an infinitesimally small region in the fluid through, and within which, some property of the flow is transported, produced and/or consumed (Bradshaw, 1971). For a given property (discussed in further detail below) not all effects shown in Fig. 2 may be applicable. For example, in the case of total mass at a point, there are no sources and sinks as dictated by the law of mass conservation. For a species concentration, such as mass fraction of drug in solution, the transport of this property from the tablet/liquid interface can be modeled as a boundary condition or explicitly as a mass source term. For a laminar flow, mean and turbulent transport terms collapse into one for convection. The term 'viscous' implies transport of species concentration, momentum and energy through the action of molecular exchange across the control volume surface, while body forces can include effects due to gravity. The fundamental conservation equations encapsulate the bookkeeping of the contributions to the rate of change with respect to time of a certain property inside the control volume. This 'property' is generally either one of the fundamental variables satisfying a physical conservation principle (i.e. species mass fraction, momentum and energy), or some physically related combination thereof (e.g. temperature, viscous dissipation rate, turbulence kinetic energy, Reynolds stress, vorticity, *etc.*). For each property, the result is a non-linear partial differential equation which in its full form, with a given set of appropriate inlet flow and boundary conditions, cannot be solved analytically, thereby requiring a numerical solution procedure (or 'computer simulation').

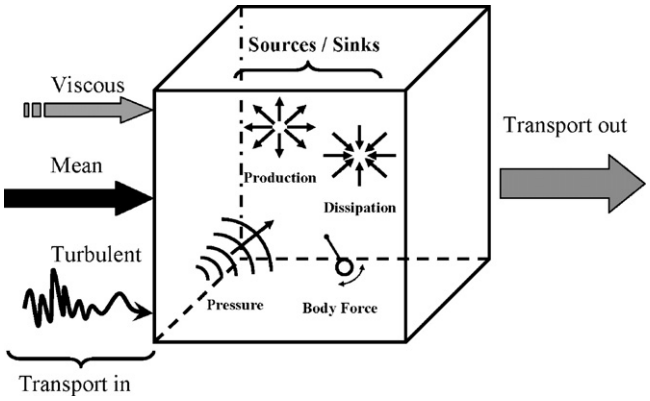


**Fig. 2.** Control volume showing physicochemical factors influencing the rate of change of some defined flow property within the volume (after Bradshaw, 1971, with permission).

Since the focus of this paper is to interpret the pharmaceutical relevance of the results obtained using CFD, the interested reader is referred to the literature (White, 1994; Bird et al., 1960; Patankar, 1980; Wendt, 1996) regarding the precise details of the derivation of the conservation equations, their discretization and subsequent numerical solution using iterative schemes.

### 2.2. Model geometry, mesh generation and boundary conditions

In practice, infinitesimally small volumes cannot be used to represent the flow domain. A mesh of finite size is generated for the region in which flow takes place, as shown in Fig. 3. The model shown in Fig. 3 was created using a separate mesh generation program, Gambit, belonging to the Fluent suite of programs. The precise dimensions for the flow-through cell were obtained using technical drawings of the Sotax vessel. Relevant sections of this are shown in Fig. 4. The tablet dimensions used in the simulations are shown in Fig. 5.

The fineness of the mesh is dictated by several factors, for example the physical scale of the flowfield, the nature of the physics that requires modeling and the accuracy needed for mesh-independent solutions. The mesh in Fig. 3 has predominantly unstructured hexahedral cells, except in the region of the 'Dissolution Test Section', where tetrahedral cells were created for convenience. In Fig. 3, the $Z$-axis passes along the centre line of geometry and its origin, labeled as $(X_0, Y_0, Z_0)$, is anchored precisely 1 mm below the 'Flow inlet' (shown in green). Unless stated otherwise, all distances are quoted relative to this frame of reference. A fine mesh of prismatic cells is layered around the tablet to resolve the velocity boundary layer around it (not shown in Fig. 3). Eight such layers are defined with the very first at a distance of 0.04 mm from the tablet surface. Since the examination of wall shear stress distributions around the tablet will form an important measure of the tablet erosion, it is imperative to have a fine mesh around the tablet, since the wall shear stress is directly proportional to the local velocity gradient.

In going from the real geometry to the simulation model several assumptions are made which simplify the setup of the model with negligible effect on the flow structures of interest. For example, Fig. 3 indicates that the tablet holder is not included since its obstruction to flow is deemed minimal based on its thickness compared to the local flow cross-section. Nevertheless, the tablet is positioned at a location as if it was being held in place by the holder. In reality, the actual location of the dosage form can be quite arbitrary (Möller, 1983), depending on its physical size and the mode of operation (open or packed column). The 'sieve and filter chamber' at the top of the cell are modeled as empty conduits. Their functions as physical barriers are not modeled since their primary effect in a simulation is to contribute to additional pressure drop in the flow downstream of the region of interest, namely everything up to and including the tablet. Qualitatively this assumption has no effect on the flow patterns because the pressure at the outlet is fixed at atmospheric (zero bar gauge pressure), consequently if the effect of the filters had been modeled, the additional pressure drop in the system would have been compensated for *in the simulation model* by increased pressure head at the inlet. In reality, the pressure the pump applies is limited, and any significant increase in backpressure created by filter blockage could affect the throughput. This is a special case that has not been studied.

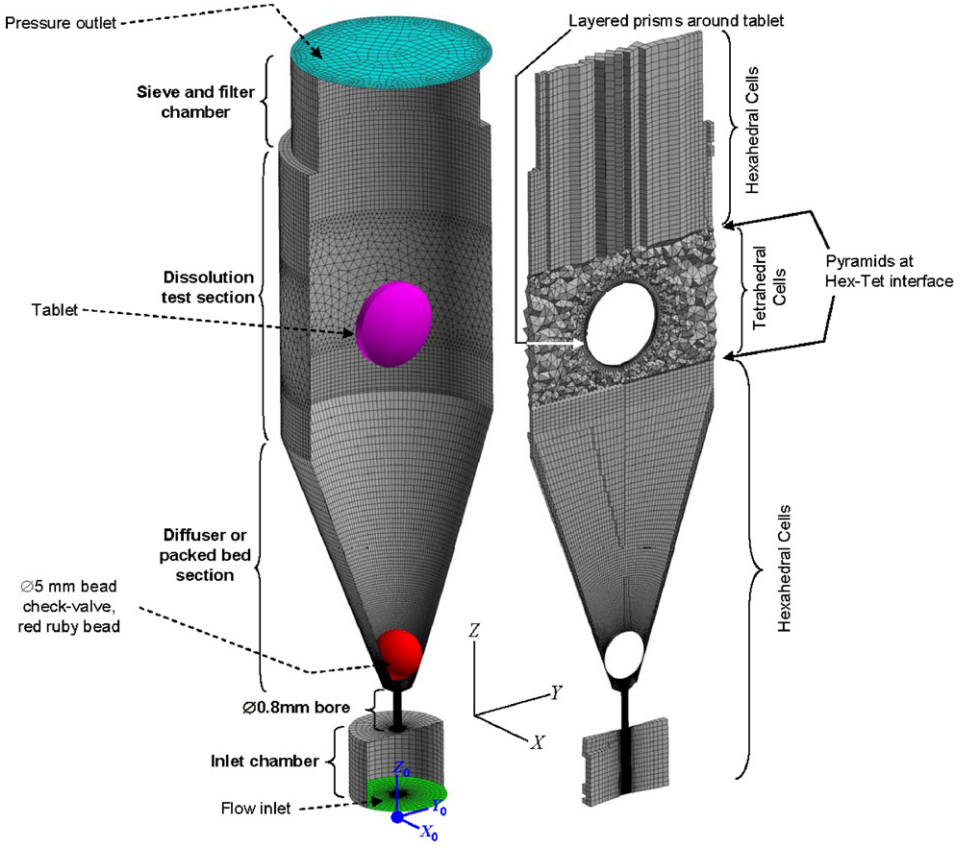


**Fig. 3.** Cut-out view of model geometry showing elements of hybrid mesh with 853,915 computational cells with the following breakdown: 79.8% hexahedra, 15.9% tetrahedral, 3.9% prisms and 0.4% pyramids. The origin of the coordinate system ($X_0$, $Y_0$, $Z_0$) is defined 1 mm below the flow inlet. (For interpretation of the references to colour in this figure legend, the reader is referred to the web version of the article.)

In Fig. 4 the effect of the 20° chamfer at the inlet, from ∅10.4 mm to ∅9.67 mm, and the blended radius of 0.4 mm at the top inside edge of the ∅9.67 mm chamber are not modeled since their effects too are assumed to be negligible on the subsequent flow through the sudden contraction of the ∅0.8 mm bore. Consequently, the real blended radius is treated in the model as a sharp corner and the model flow inlet is situated at the ∅9.67 mm plane. At the flow inlet it is assumed that a top hat, or rectangular, velocity profile can be specified. Two pulsating profile forms were specified that deliver the same average discharge rate of fluid (Kakhi, 2009). The rationale behind this is to determine how the mechanical shearing of the tablet is influenced by a change in the sinusoidal profile. Only the

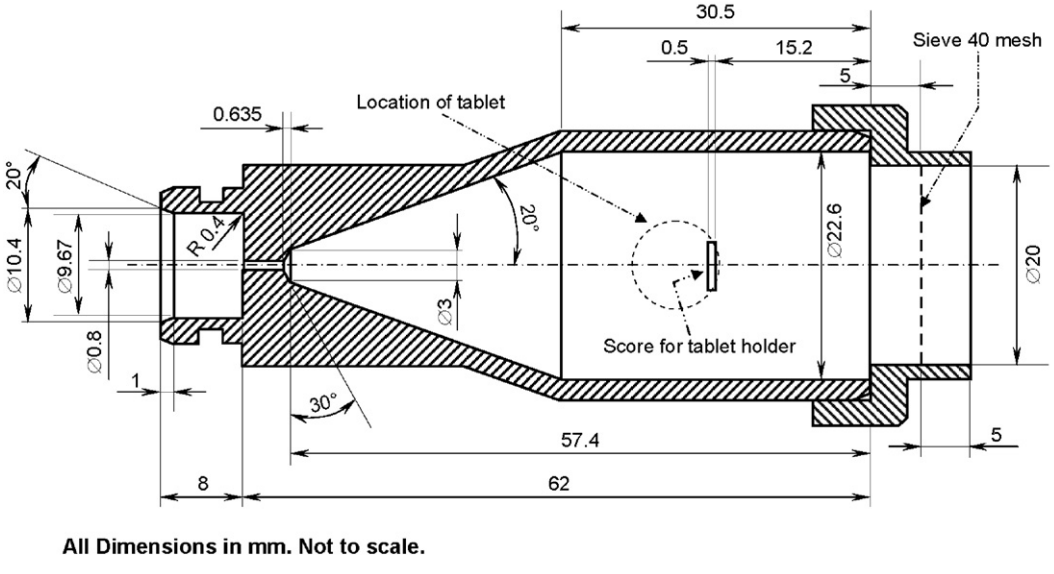


**Fig. 4.** Dimensions for the ∅22.6 mm flow-through cell, reproduced/adapted with permission of Sotax Group, 411 Caredean Drive, Horsham, PA 19044-1316, USA. The tablet is located along centre-line of geometry, and its midpoint is 51 mm above the ∅10.4 mm inlet. This is not an official technical drawing, but includes all salient dimensions required for the model generation.

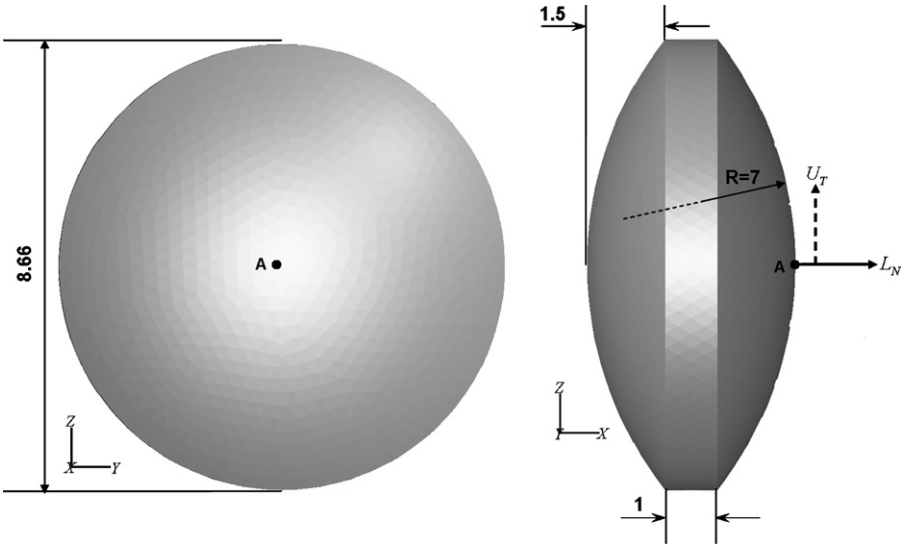


**Fig. 5.** Front and side view of tablet used in calculations. Tablet dimensions are in mm. $L_N$ is the wall-normal distance from point A and $U_T$ is the velocity orthogonal to $L_N$. Point A is located at the surface of the tablet where $X = 2$ mm, $Y = 0$, $Z = 51$ mm relative to the origin of the coordinate system $(X_0, Y_0, Z_0)$ defined in Fig. 3.

functional relations are specified below and depicted graphically in Fig. 6. Based on a comparison with data from the pump manufacturer (Kakhi, 2009), Eq. (1) fits the sinusoidal specification of a pure sinus half-wave profile (Langenbucher et al., 1989)

$$\dot{V}_1 = \begin{cases} \pi N_s V_{\max} \sin(2\pi N_s t) & \text{Pump Discharge} \\ 0 & \text{Pump Suction} \end{cases} \quad (1)$$

$$\dot{V}_2 = \begin{cases} 2N_s V_{\max} [1 - \cos(4\pi N_s t)] & \text{Pump Discharge} \\ 0 & \text{Pump Suction} \end{cases} \quad (2)$$

Fig. 6 shows that in spite of the same average delivery rate, the instantaneous discharge rate profiles differ in their peak values by 28% (normalized relative to the peak value, $\dot{V}_{1,\max}$, based on Eq. (1)). In order to place this percentage difference into perspective, the current USP standard (United States Pharmacopeia, 2008) allows for ±5% variation in the nominal (average) flow rate and a pulsation of $120 \pm 10$ pulses/min. Thus, an average flow rate of 16.8 ml/min at 110 pulses/min is also acceptable, which, when compared to 16 ml/min at 120 pulses/min, would yield a 15% difference in $\dot{V}_{1,\max}$. Therefore a change in the instantaneous profile for a given average flow rate and pulsation frequency can generate a larger offset than that allowed for in the compendial specification. A more mathematically precise characterization of the inlet flow is needed than what is stated in the compendia.

All the calculations were performed with spatial differencing schemes having second order accuracy with a first order implicit time stepping formulation. The primary focus of this study was the first 0.25 s of pump discharge into the flow-through cell. A time step of 0.25 milliseconds was chosen. Convergence of the iterative scheme was verified using a three-pronged approach, namely achieving an overall mass imbalance between inlet and outlet less

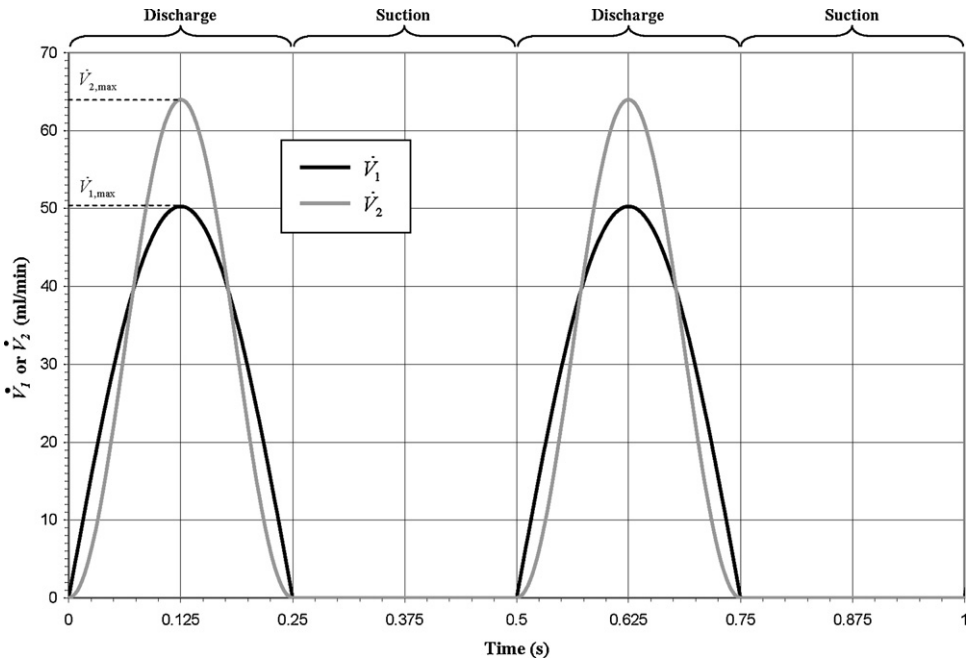


**Fig. 6.** Discharge (volumetric flow) rate of dissolution medium into flow-through cell ($\dot{V}_1$ and $\dot{V}_2$) at $\langle \dot{V} \rangle = 16$ ml/min. One complete stroke lasts 0.5 s.

than typically 0.01%, reduction of residuals by at least three orders of magnitude and constancy of the flow field variables (such as pressure and vector components of velocity) at key locations in the geometry where large gradients are expected. Calculations were also performed to ensure that results were generally grid and time step independent. In this regard a balance is very often struck between the practical limitations associated with the hardware capabilities and the ability to predict the flow field features of interest. The choices made in this context can only really be validated if the simulation work is complemented with experimental measurements which demonstrate whether the predictions are on the right track.

### 2.3. Operational modes investigated

Three separate cases are analyzed in this paper, namely:

- Dissolution cell operated without any beads (i.e. no ⌀5 mm red ruby bead (Sandoz Fils SA, 2008) and no ⌀1 mm glass beads (Sigmund Lindner GmbH, 2008)); this is henceforth referred to as the 'no-beads' calculation.
- Dissolution cell operated in open-column mode (only ⌀5 mm red ruby bead present).
- Dissolution cell operated in packed column mode (⌀5 mm red ruby bead and the ⌀1 mm glass beads present).

For all calculations the physical properties of water at 35 °C, 1 bar were specified (VDI Wärmeatlas, 1991).

### 2.4. 'No-beads' calculation

The 'no-beads' calculation in the ⌀22.6 mm apparatus for tablets appears to have a limited scope of application. Procedures without any beads have been suggested in the past for special cases where increased mechanical agitation is required to achieve accelerated dissolution, for example in oral osmotic systems (Langenbucher et al., 1989). However, this test case serves as a useful reference condition against which the other modes of operation can be compared.

### 2.5. Open-column mode calculation

Simulation of the open-column configuration proved to be a particularly challenging task since the motion of the red ruby bead (referred to simply as the 'bead' in the following discussion) had to be incorporated in the model. In theory, this is akin to a flow/check-valve problem. One of the primary functions of the bead is to prevent the contents of the cell from emptying when it is removed from its housing (Langenbucher et al., 1989; Magnier, 2008). In addition to this practical function, it also helps to disperse the jet emerging from the ⌀0.8 mm bore so that the dosage form is not exposed to a narrow, high-velocity stream of fluid (Bhattachar et al., 2002). Ideally, a CFD model for this test case would treat the fluid–bead interaction without the need to prescribe the bead movement explicitly as a boundary condition. In other words, as in the real-life application, the bead should move with all its degrees of freedom (three translational and three rotational) because it experiences a resultant force and moment acting on it from the motion of the fluid flowing past it. Initial tests with the Fluent solver using very fine meshes in only two dimensions demonstrated that unstable and physically implausible pressure fields were predicted with water as the fluid medium (Hu, 2007), whereas the use of a compressible medium, such as air, did yield potentially physical results. It therefore became necessary to construct a model in which the bead movement was an explicit input to the model. Since the movement of the bead in reality is a result of the discharged fluid imparting a portion of its kinetic energy to lift it, this loss of kinetic energy would not be captured in the current model, since the fluid now 'sees' the bead as an obstacle (albeit moving) around which it is forced to flow. Since the motion of the bead is dominated by translational movement along the $Z$-axis, the other degrees of freedom were ignored. Before the bead movement can be specified in terms of a mathematical expression, the extent of the bead displacement, or *lift*, has to be known.

Fig. 7(a) illustrates the local mesh along $X = 0$ and various planes of constant $Z$ in the vicinity of the bead, while Fig. 7(b) is an expanded view from the top of the bead and a plane cut of the mesh between the vessel wall (20° half-angle frustum) and the midsec-

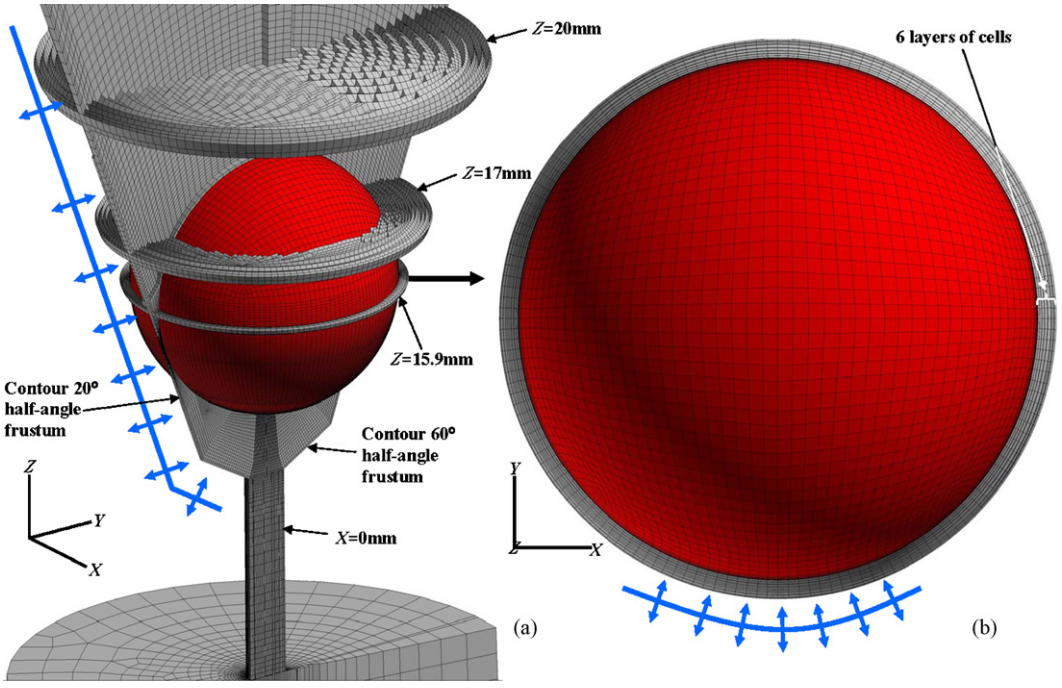


**Fig. 7.** Mesh in the vicinity of the red ruby bead. (a) Plane cuts along $X = 0$ and various $Z$ = constant. (b) Expanded view from the top of the local mesh at the midsection of the red ruby bead. Blue line and arrow annotations schematically indicate region of mesh layering.

**Table 1**
Bead lift as a function of peak discharge rate, $\dot{V}_{2,\max}$, based on relation $\dot{V}_2$ (Eq. (2)). The column showing $\langle\dot{V}\rangle$ represents the corresponding average flow rates for reference purposes only.

| $\dot{V}_{2,\max}$ (ml/min) | $\langle\dot{V}\rangle$ (ml/min) | $L_{p,max}$ (mm) |
|---|---|---|
| 64 | 16 | 0.45 |
| 32 | 8 | 0.36 |
| 16 | 4 | 0.26 |

tion of the bead in its rest state. Normally the bead would be in touch with the side walls of the 20° half-angle frustum at $Z$ = 14.9 mm. This would imply that any mesh would have cells that go to zero width at that location. The moving-deforming-mesh (MDM) algorithm in Fluent requires cells to have a finite width, albeit small. Therefore, an initial clearance has to be defined to avoid numerical difficulties. In the present model the initial clearance between the bead and the adjacent wall was chosen to be 0.014 mm, which is small compared to the bead dimension (⌀5 mm) and its lift (discussed below). This region is meshed with six cells. However, as the bead moves up, the MDM algorithm adds cells into and simultaneously removes cells from the computational domain so that existing cells do not exceed (or fall under) a certain width. In essence, the bead is not moving, but rather the mesh around it is shifting. The blue line annotations in Fig. 7(a) and (b) indicate the extent of the region over which the 'mesh layering' occurs. This encompasses the entire inner surfaces of the 20° and 60° half-angle frustums and the plane $Z$ = 44.25 mm (not shown for reasons of scaling). Referring to Fig. 3, $Z$ = 44.25 mm is the plane below the tablet where the mesh of hexahedral cells interfaces with the pyramids. The bi-directionality of the arrows emphasizes that cells are added or removed depending on whether the bead is moving up or down. In such an approach the number of cells in the computational domain changes. For example, the calculation starts with 853,915 cells and by the time the bead reaches its maximum lift height, the mesh size increases to 1,873,275 cells.

To determine the bead lift at the peak discharge rate relative to its rest state (defined as the condition during the pump's suction stroke), a user defined function supplied by Ansys Inc. was employed. The procedure calculates the lift force on the bead generated by the pressure field due to the flow, and compares this lift force to the bead's weight. If there is an imbalance the mesh is moved in prescribed increments in the direction of the resultant force. By refining the incremental movement, a convergence towards an equilibrium lift height can be established, since at that location the lift force will just balance the weight of the bead. Using this procedure the results presented in Table 1 were obtained based on the peak discharge rate defined in terms of the velocity profile $\dot{V}_2$, Eq. (2). A bead displacement–time relationship is postulated which takes the following form:

$$L_p = \begin{cases} 1/2L_{p,\max}\,[1-\cos(4\pi N_s t)] & \text{Pump Discharge} \\ 0 & \text{Pump Suction} \end{cases} \quad (3)$$

Differentiating Eq. (3) with respect to time yields the bead velocity profile:

$$U_p = \begin{cases} 2\pi N_s L_{p,\max}\sin(4\pi N_s t) & \text{Pump Discharge} \\ 0 & \text{Pump Suction} \end{cases} \quad (4)$$

Both of these relations are shown graphically in Fig. 8.

### 2.6. Packed column calculation

The simulation of the flow field in the packed column configuration does not geometrically resolve the presence of the ⌀1 mm glass beads. The region of the packed column typically contains about 5200 glass beads (based on an average of 30 separate measurements (Gao, 2006)). Having a computational mesh which resolves a random packing of so many solid elements was simply not feasible within the scope of the present study. Instead, the region of the packed column was assumed to be a porous zone. When making such an assumption, it is no longer possible to resolve the tortuous path the flow has to take through the interstices/pores of the random packing of glass beads. Such a 'black box' approach is acceptable if the tablet is placed well above the densely packed region of the beads. If, however, the dosage form is embedded or dispersed in the packed bed, as is the case with powders (Bhattachar et al., 2002), detailed simulation of the flow through the pores would be required. A further consideration is the case of a tablet placed directly on the bed of beads. At the level of the topmost ⌀1 mm glass beads, the velocity profile emerging from the bed is uniform in the centre, but peaks just before the wall and then drops off sharply to zero according to the no-slip condition (Schwartz and Smith, 1953). This localized non-uniformity in the velocity profile can only be predicted by a detailed model which resolves the glass beads as geometrical physical obstructions.

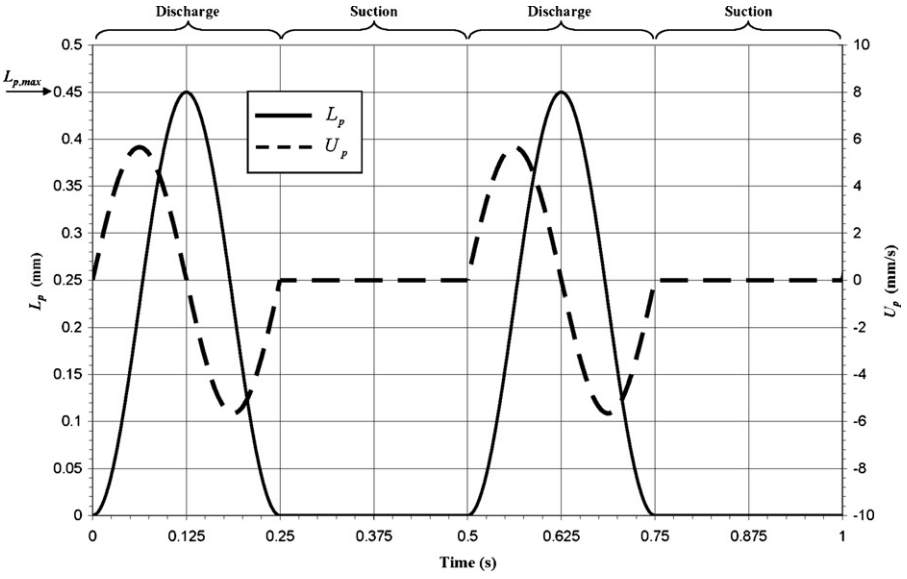


**Fig. 8.** Bead displacement ($L_p$) and velocity ($U_p$) profiles as function of elapsed time, based on Eqs. (3) and (4).

In the porous zone model the velocity field is calculated by including source terms in each component of the momentum equation representing the viscous and inertial drag forces imposed by the porous zone on the fluid. The source terms take the following form (Fluent, 2006):

$$S_i = -\left( \underbrace{\frac{\mu}{\alpha} u_i}_{\text{Viscous Loss Term}} + \underbrace{C\frac{1}{2}\rho|u|u_i}_{\text{Inertial Loss Term}} \right) \quad (5)$$

The empirical constants ($1/\alpha$ and $C$) in Eq. (5) are chosen such that the predicted pressure drop across the porous zone matches the value obtained from experimental observation. Eq. (5) is expressed in vector notation, in other words the index $i$ corresponds to each of the principal flow directions ($i = 1$, 2 and 3 corresponding to $X$, $Y$ and $Z$ respectively), and it assumes that the coefficients $1/\alpha$ and $C$ are constant throughout the porous zone. In this study the loss resistance coefficients are estimated by making recourse to the Ergun equation, expressed below in terms of the Blake-type friction factor (Ergun, 1952):

$$f = \frac{150}{Re'} + 1.75 \quad (6)$$

Eq. (6) involves two dimensionless groups, the friction factor $f = (\Delta P/h)(d_{eff}/\rho U_s^2) \cdot [\varepsilon^3/(1-\varepsilon)]$ and a modified Reynolds number, defined as, $Re' = \rho U_s d_{eff}/\mu(1-\varepsilon)$. The voidage fraction (or porosity) of a bed of particles, $\varepsilon$, is the fraction of the bed volume which is occupied by the space between the solid particles, i.e. the volume fraction of the fluid flowing through the interstices of the bed. It can be approximated in terms of the bulk and material density (Howard, 1989):

$$\varepsilon = \frac{V_{Bed} - V_{solid}}{V_{Bed}} \cong 1 - \frac{\rho_{bulk}}{\rho_{solid}} \quad (7)$$

$V_{Bed}$ is the volume occupied by the ⌀1 mm glass beads (including the interstitial spaces) when randomly packed in the dissolution cell. $V_{solid}$ represents just the material volume of all the beads. For the 1 mm glass beads, $\rho_{solid}$ ~2500 kg/m$^3$ and hence using Eq. (7), $\varepsilon = 0.35$ is obtained, which falls into the lower end of the experimental range in randomly packed beds for uniformly sized particles (Kunii and Levenspiel, 1991). The actual porosity can be expected to be slightly higher due to the expansion the bed experiences when dissolution medium is pulsed through it. The precise value of $\varepsilon$ has negligible effect on the qualitative characteristics of the flow downstream of the packed bed, but instead influences the pressure drop across it; the latter effect is not the focus of the present study. By comparing Eqs. (5) and (6), and noting that resistance coefficients for porous media in Fluent are calculated in terms of the superficial velocity, it can be shown that:

$$\alpha = \frac{d_{\varnothing 1\text{mm}}^2}{150} \frac{\varepsilon^3}{(1-\varepsilon)^2} \quad (8)$$

$$C = \frac{3.5}{d_{\varnothing 1\text{mm}}} \frac{(1-\varepsilon)}{\varepsilon^3} \quad (9)$$

Given that the packed column calculation ignores the geometrical presence of the spherical beads, the associated computational mesh contains neither the ⌀1 mm glass beads nor the ⌀5 mm red ruby bead in their respective physical forms. Therefore, the hybrid mesh used for this calculation, involving 1,370,174 cells, is exactly the same as the one required for the 'no-beads' calculation. There is also no mesh movement to prescribe, since most of the packed column is immobile at the standard flow rates of 4, 8 and 16 ml/min, except for the red ruby bead and the ⌀1 mm glass beads in its very immediate vicinity.

## 3. Results and discussion

### 3.1. Test case: 'no-beads' calculation

Fig. 9 presents contour plots of the magnitude of the $Z$- and $Y$- (i.e. the in-plane) components of the velocity vector along the coordinate surface $X = 0$ for a laminar flow pulsed at $\langle \dot{V} \rangle = 16$ ml/min according to Eq. (2). The contour plots are all scaled to the same color coding shown in the legend. The results have been presented at three different time levels during the discharge stroke of the pump which lasts 0.25 s; the results at $t = 0.0625$ s and $t = 0.1875$ s are spaced out evenly about the peak of the pulse which occurs at

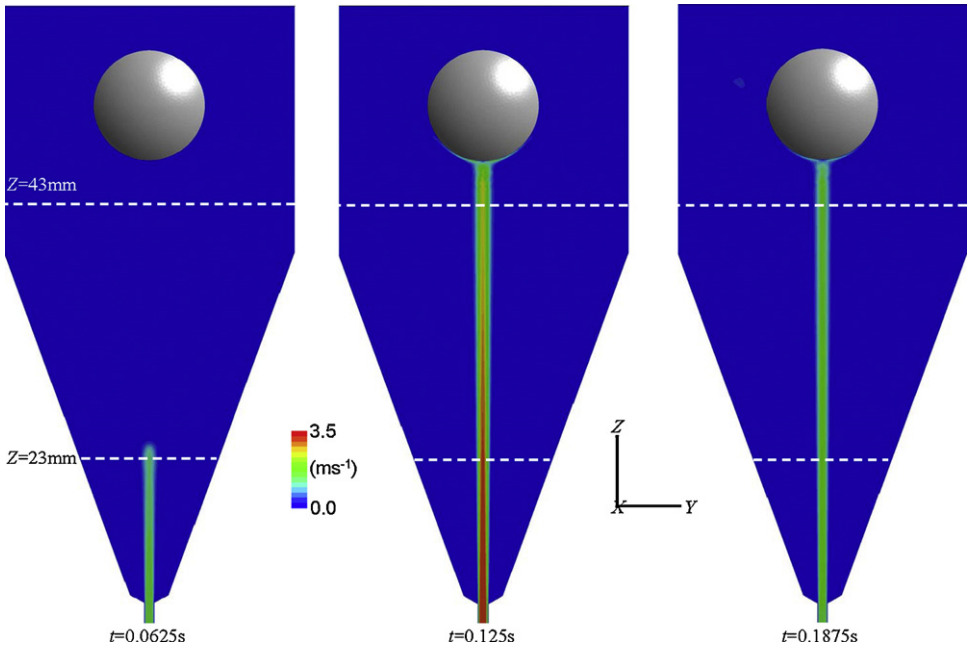


**Fig. 9.** 'No-beads' calculation. Filled contour plot of (in-plane) velocity magnitude along the section $X = 0$ at equally spaced time intervals during the pump discharge stroke. $\langle \dot{V} \rangle = 16$ ml/min. Instantaneous velocity based on relation $\dot{V}_2$ (Eq. (2)).

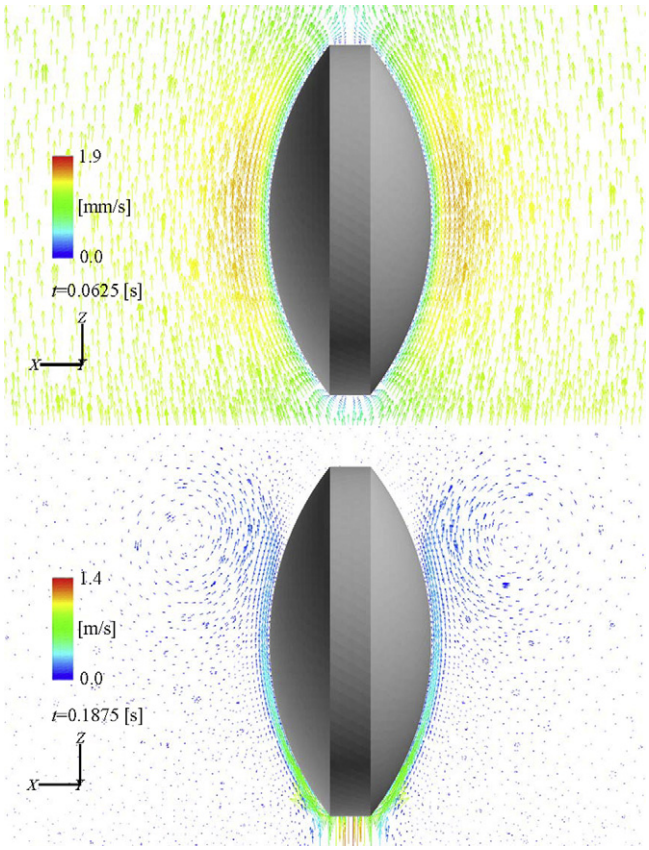


**Fig. 10.** 'No-beads' calculation. *Z*–*X* components of the velocity vector field colored with its local in-plane magnitude at $t = 0.0625$ s and $t = 0.1875$ s. $\langle \dot{V} \rangle = 16$ ml/min. Instantaneous velocity based on relation $\dot{V}_2$ (Eq. (2)).

$t = 0.125$ s. Given that the discharge profile $\dot{V}_2$, shown in Fig. 6, is a symmetrical pulse (about $t = 0.125$ s) this means that the velocities at the inlet to the model at $t = 0.0625$ s and $t = 0.1875$ s are the same.

Fig. 9 emphasizes why the red ruby bead is needed from a fluid dynamics perspective. Without it, a jet of high-speed dissolution medium passes through the geometry and impinges on the tablet. The resulting flow field has a very non-uniform velocity profile. At $t = 0.0625$ s the jet has not yet reached the tablet, in stark contrast to the situation at its symmetric counterpart ($t = 0.1875$ s). Fig. 10 reinforces this observation with in-plane velocity vector components colored by the in-plane velocity magnitude in the vicinity of the tablet. The vector plot at $t = 0.0625$ s indicates a uniformly distributed velocity profile approaching the tablet, but the velocity scale is of the order of m ms$^{-1}$, while at $t = 0.1875$ s a narrow jet impinges on the tablet with velocities three orders of magnitude higher. This significant difference manifests itself upon examination of the tablet (wall) shear stress, as shown in Fig. 11. The tablet shear stress, $\tau_w$, represents the magnitude of the stress tensor components acting on an elemental solid surface. The normalization shown in Fig. 11, in terms of $\tau_{max} = 0.011$ Pa, is used for comparison with the results from the two remaining test cases to be discussed further on. The quantity $\tau_{max}$ is the largest value of $\tau_w$ predicted in the open and packed column calculations. This gives some idea of the severity of the flow in the 'no-beads' test case with ratios of $\tau_w/\tau_{max} \approx 6000$. The local minimum in $\tau_w$ at the bottom of the tablet coincides with the stagnation point where the flow impinges orthogonally on the tablet. The shear stress distribution shown in Fig. 11 assumes the tablet is not displaced by the highly non-uniform, high-velocity impinging jet. In practice, this may not be the case depending on the dosage form's density. As pointed out earlier, this test case serves as a 'thought experiment' against which the standard operational modes can be compared.

According to the legend scaling in Fig. 9, at $t = 0.125$ s the peak velocity along the centerline of the jet is greater than 3 ms$^{-1}$ for much of its length until the spreading of the jet through entrainment of surrounding fluid and impingement on the tablet gradually reduce it. The difference in spreading rate distinguishes a turbulent jet from a laminar jet. Based on the conclusions of a previous study examining the flow regimes in this dissolution device (Kakhi, 2009), a calculation of a turbulent flow is only meaningful in the case of the 'no-beads' configuration at average flow rates greater than 16 ml/min because the progress of the high-speed jet is not arrested by the beads. To verify this assertion, measurements of the actual spreading rate of the jet would be required. To emphasize the contrast in behaviour to the laminar state, the results of modeling the flow with a turbulence model are also shown. In this work the '$k$–$\omega$' model (Wilcox, 2004) with a low Reynolds number correction is employed, the description of which is beyond the intended scope of this paper. Experience with the $k$–$\omega$ model has shown that within the framework of two-equation models of turbulence, better agreement with experimental measurements in certain flow configurations can be obtained compared with the classical '$k$–$\varepsilon$' model

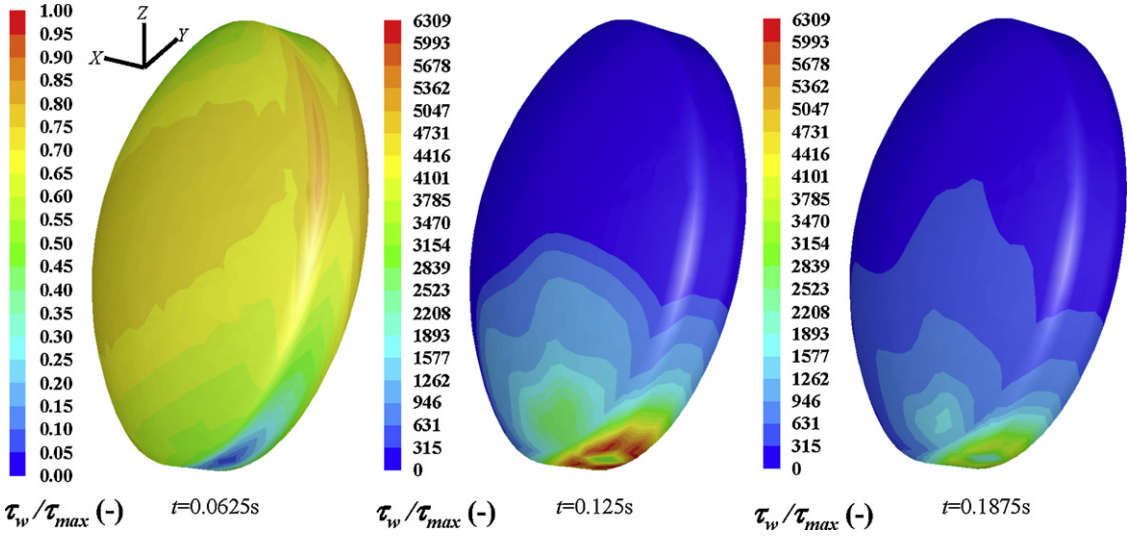


**Fig. 11.** 'No-beads' calculation. Contour plot of tablet shear stress, $\tau_w$, normalized with $\tau_{max} = 0.011$ Pa. $\langle \dot{V} \rangle = 16$ ml/min. Instantaneous velocity based on relation $\dot{V}_2$ (Eq. (2)).

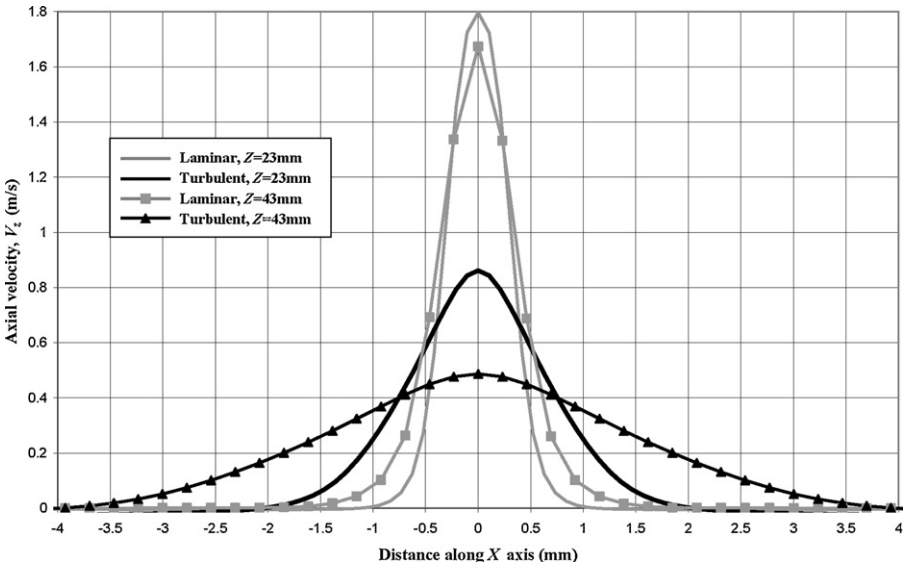


**Fig. 12.** 'No-beads' calculation. Comparison of the axial ($Z$-component) velocity profiles for a laminar and turbulent ($k$–$\omega$ model) jet along $Y = 0$ at two different $Z$-sections ($Z = 23$ and $Z = 43$ mm) for $t = 0.1875$ s. $\langle \dot{V} \rangle = 16$ ml/min. Instantaneous velocity based on relation $\dot{V}_2$ (Eq. (2)).

(specifically in this context $\varepsilon$ denotes the viscous dissipation rate of turbulence kinetic energy, and not voidage). The correct choice for a turbulence model is best verified by experimental validation.

Fig. 12 shows profiles of the axial velocity, more precisely the $Z$-component of the velocity vector, at two separate planes ($Z = 23$ and 43 mm) along a line where $Y = 0$. The annotations in Fig. 9 indicate where the aforementioned $Z$-planes are located. The abscissa is in the range $-4 \leq X \leq 4$ because the origin of the coordinate system ($X_0$, $Y_0$, $Z_0$), shown in Fig. 3, is defined along the centerline of the geometry. The corresponding profiles along the line $X = 0$ have been omitted in Fig. 12 for clarity, although they overlap virtually indistinguishably from the curves currently depicted, thereby demonstrating that the profiles are symmetrical about the $Z$-axis. The stark contrast in jet spreading rates (manifested by the width of the jet) between the laminar and turbulent test cases is an indication of how turbulence enhances cross-flow mixing.

### 3.2. Open column configuration

In this mode of operation it is quite common for the test specimen either not to be placed in the tablet holder or not to remain there as dissolution progresses. A case in point is the drug-eluting stent which is sometimes placed obliquely in the column. It is therefore of interest to analyze the uniformity of the velocity field beyond the red ruby bead. Figs. 13–16 present the results of velocity contour plots of the $Z$-component of velocity on five different coordinate surfaces. Four of these, namely $Z = 14$, 16, 18 and 20 mm have been horizontally displaced from their original positions (centered on $X = Y = 0$) in order to enhance the clarity of the figures. Each coordinate surface cut has its own color legend, scaled to the local minimum and maximum of the $Z$-component of velocity. Given the significant change in velocity in the space of a few millimeters along the $Z$-axis, a single color scale would hide the detail in the flowfield characteristics for all the $Z$-plane cuts. The red ruby bead and a wall section (shaded in grey) are also shown purely for illustrative enhancement of the underlying flow field physics.

Fig. 13 shows how the high jet velocity of 1.8 $\mathrm{ms}^{-1}$, created as a result of the sudden contraction through the ⌀0.8 mm bore, impinges on the bead. The jet is then redirected into regions of recirculating flow (as evidenced by the negative local minimum of the corresponding color legends at $Y = 0$ and $Z = 14$ mm) and further up the column. At $Z = 16$ mm the velocity maximum drops to 20 cm/s because the area available for flow (relative to the ⌀0.8 mm bore) has increased by an order of magnitude. It is a region of high velocity gradients since the flow is bounded by the 20° half-angle frustum and the bead over a small clearance. A no-slip boundary condition is applied at all walls, in other words a zero *relative* velocity between a wall surface and the fluid directly adjacent to it. Consequently, the fluid directly in contact with the bead moves at the local bead velocity, as indicated, for example, by the non-zero velocity along the inner annulus of plane $Z = 18$ mm in Fig. 13. The fluid adjacent to the stationary frustum wall has zero velocity. In the same figure, the plane cuts at $Z = 16$, 18 and 20 mm suggest that the entire flow is now directed in the positive $Z$-direction. At $Z = 20$ mm a relatively uniform distribution in $Z$-velocity is predicted. This is in stark contrast to the contour plots at $Z = 20$ mm at $t = 0.125$ s and $t = 0.1875$ s in Figs. 14 and 15. In particular, at $t = 0.1875$ s, during the downward movement of the bead, negative $Z$-velocities of much greater magnitude are predicted than at the two previous times. Fig. 16 depicts the state of the flow when pumped at $\langle \dot{V} \rangle = 8$ ml/min. An assumption of linear scaling (or halving of the velocities) to accommodate the reduction in the pump's delivery is clearly inappropriate when comparing the results on the planes $Z = 18$ mm and 20 mm with those at $\langle \dot{V} \rangle = 16$ ml/min in Fig. 15.

The aforementioned predictions emphasize that there are appreciable non-linear interactions taking place, resulting in a complex flowfield in the vicinity of the red ruby bead. For example, given the symmetry of the input velocity pulse (Fig. 6) and the fact that at $t = 0.0625$ s and $t = 0.1875$ s the jet issuing from the ⌀0.8 mm bore should have the same characteristics, the resulting flow fields just downstream of the red ruby bead are entirely different. This is in part due to the interaction of the fluid with the red ruby bead which is moving in opposing directions at these two times. To clarify the broader significance of this observation in terms of how the flow would potentially affect a dosage form, Figs. 17 and 18 present the velocity profiles along the planes $Z = 23$ and 43 mm (respectively). The locations of these two planes are illustrated in Fig. 9. The profiles have been plotted along $Y = 0$ and $X = 0$ to highlight the degree of asymmetry (if any) in the $Z$-component of velocity. Fig. 17 shows that in the initial phases of the pulse ($t \approx 0.0625$ s) the velocity profile is both uniform and symmetrical. However, as the pulse builds up the deviation from the predicted behaviour at $t = 0.0625$ s increases and at $t = 0.1875$ s, a very non-uniform and asymmetric profile is obtained. Further cycles of the pulse would have to be cal-

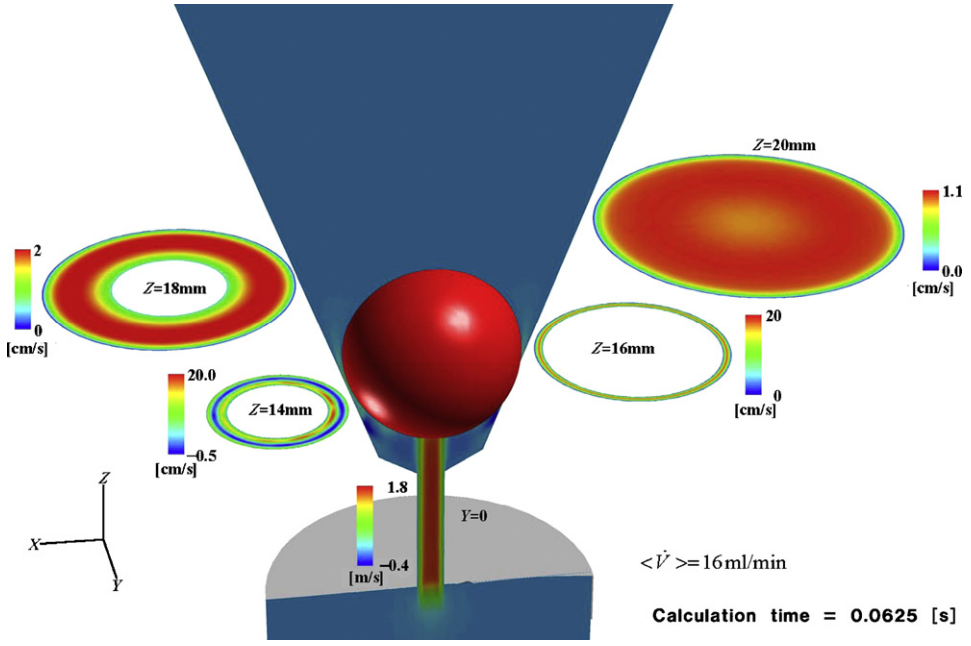


**Fig. 13.** Open column calculation. Contour plot of the $Z$-component of velocity along the plane $Y = 0$ and four planes of constant $Z$ at $t = 0.0625$ s. $\langle \dot{V} \rangle = 16$ ml/min. Instantaneous velocity based on relation $\dot{V}_2$ (Eq. (2)).

culated in order to ascertain how repeatable this prediction is. In order to calculate two sequential pulses (or discharge strokes from the pump) at least 0.75 s of physical flow time would have to be calculated. This objective was not pursued in the open-column configuration since the calculation of just one discharge stroke required about eight weeks of computation on a Dell Precision 670n workstation with a 3.6 GHz Intel Xeon processor. According to Fig. 18, the flow non-uniformities appear to level out quite significantly. This implies that ahead of the tablet a fairly flat and symmetric velocity profile is predicted. It is particularly interesting to note that at $Z = 43$ mm the velocity profiles at $t = 0.0625$ s and $t = 0.1875$ s are now far more comparable. The slight depression near the centre-line of the velocity profiles in Fig. 18 is due to the retardation effect associated with the proximity of the tablet. This is typically observed in low Reynolds number flows (White, 1994) where the viscous region is very broad and extends far ahead of the obstacle.

Given the result in Fig. 18, which indicates that just prior to the tablet the velocity profiles at $t = 0.0625$ s and $t = 0.1875$ s are very similar, $\tau_w$ in Fig. 19 at $t = 0.0625$ s and $t = 0.1875$ s are remarkably dissimilar. Since this phenomenon is also observed in the packed column calculation, its discussion is deferred to the next section. Note that in the case of the 'no-beads' calculation, Fig. 11, the difference in $\tau_w$ at the aforementioned times was attributed to the appreciable difference in the respective velocity profiles just ahead

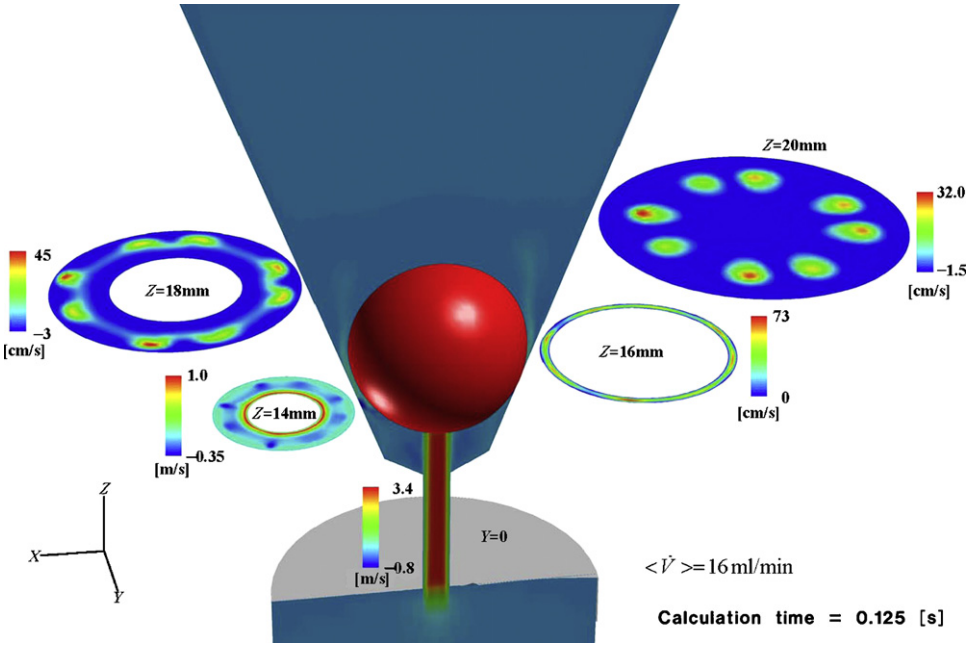


**Fig. 14.** Open column calculation. Contour plot of the $Z$-component of velocity along the plane $Y = 0$ and four planes of constant $Z$ at $t = 0.125$ s. $\langle \dot{V} \rangle = 16$ ml/min. Instantaneous velocity based on relation $\dot{V}_2$ (Eq. (2)).

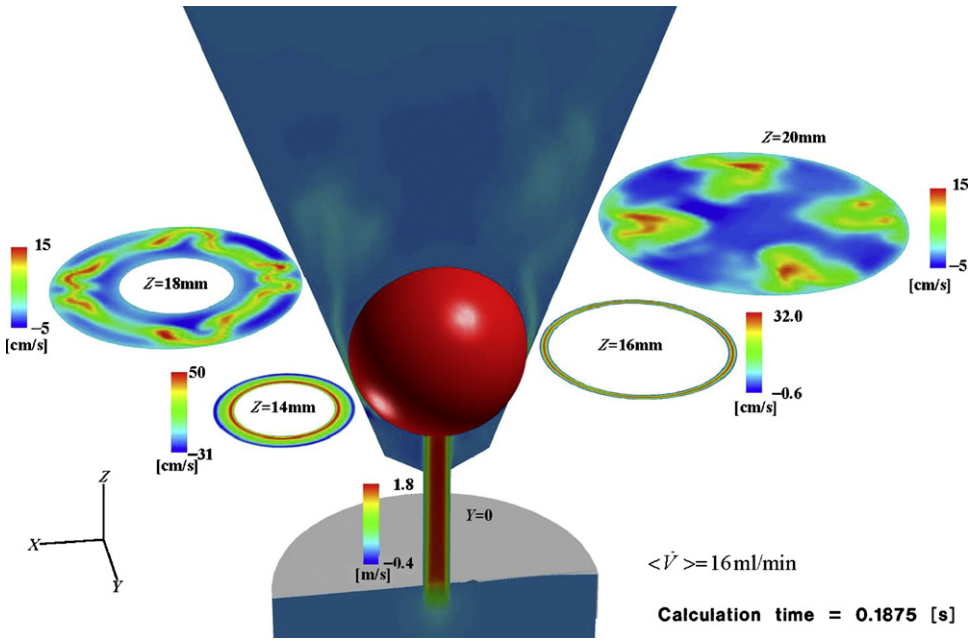


**Fig. 15.** Open column calculation. Contour plot of the $Z$-component of velocity along the plane $Y = 0$ and four planes of constant $Z$ at $t = 0.1875$ s. $\langle \dot{V} \rangle = 16$ ml/min. Instantaneous velocity based on relation $\dot{V}_2$ (Eq. (2)).

of the tablet, whereas in the open column configuration the velocity profiles at the same times are very similar. In Fig. 19, $\tau_w$ reaches a maximum towards the middle of the tablet. This is because the fluid accelerates as it moves around the curvilinear surface of the tablet, reaching its peak value at the local maximum of the curved surface. Another interesting result in Fig. 19 is the overall similarity in $\tau_w$ at $t = 0.0625$ s and $t = 0.125$ s, although the average flow velocities differ approximately by a factor of two. Fig. 20 explains this apparent similarity of $\tau_w$ in terms of the velocity profile in the near-wall region of the tablet. The velocity boundary layer reaches the free-stream value to within 1 mm from the tablet surface. Although the free-stream velocity at $t = 0.125$ s ($\langle \dot{V} \rangle = 16$ ml/min) is more than double the value at $t = 0.0625$ s, the boundary layer thickness at $t = 0.125$ s has also increased. Consequently, the velocity gradient near the tablet surface at $t = 0.125$ s ($\langle \dot{V} \rangle = 16$ ml/min) is only slightly greater than at $t = 0.0625$ s. Based on 'standard' results for *steady* laminar boundary layers developing on a *flat-plate*, the boundary layer thickness is *inversely* proportional to the square root of the mean free-stream velocity (White, 1994). However, this 'standard' result does not apply in the present situation, since the free-stream flow is clearly not steady but pulsating. In addition, the flow is taking place over a curvilinear surface, not a flat plate. The predicted distribution of $\tau_w$, when the dissolution medium is pulsed at $\langle \dot{V} \rangle = 8$ ml/min, agrees with the intuitive expectation that the shear

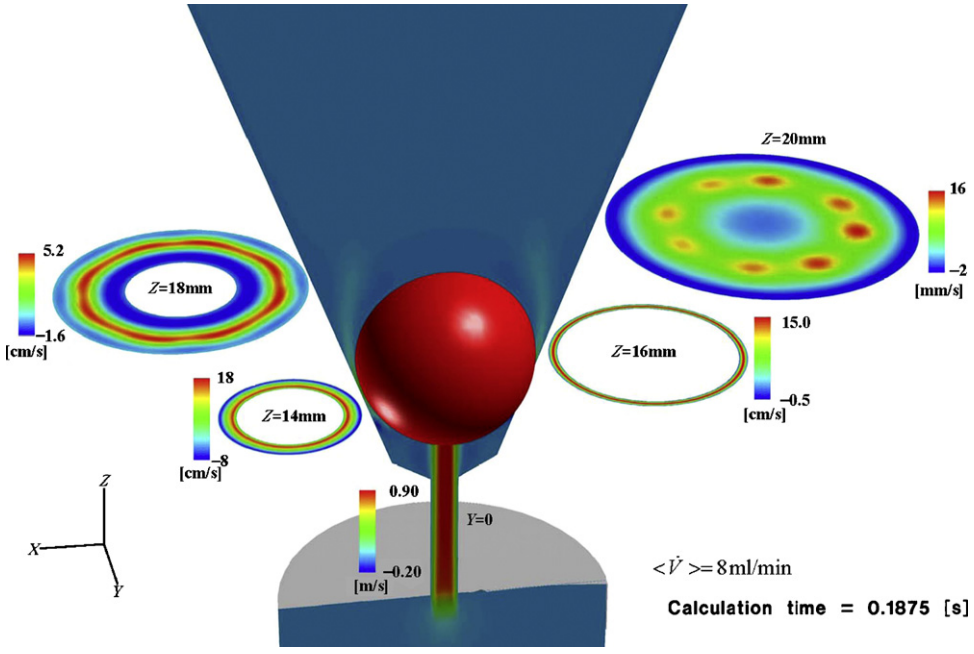


**Fig. 16.** Open column calculation. Contour plot of the $Z$-component of velocity along the plane $Y = 0$ and four planes of constant $Z$ at $t = 0.1875$s. $\langle \dot{V} \rangle = 8$ ml/min. Instantaneous velocity based on relation $\dot{V}_2$ (Eq. (2)).

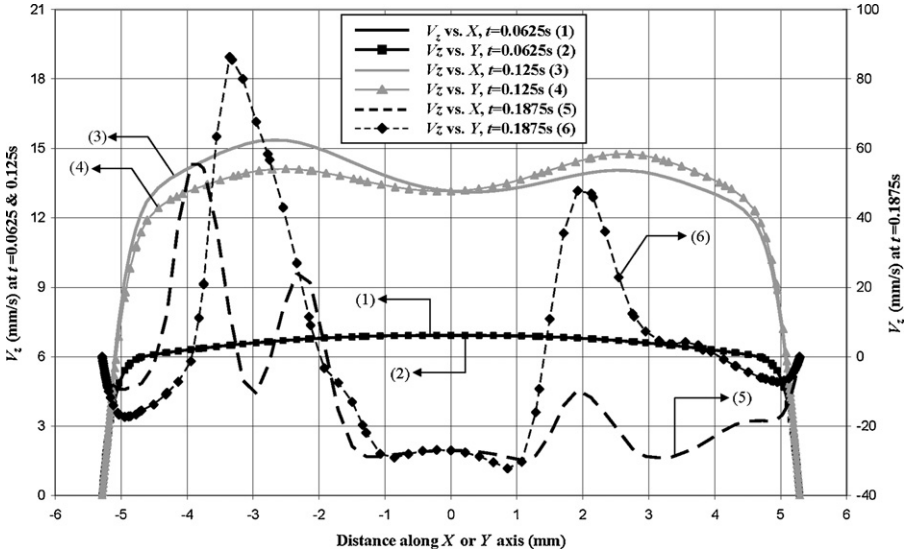


**Fig. 17.** Open column calculation. Axial ($Z$-component) velocity profiles along the line $X = 0$ and $Y = 0$ at $Z = 23$ mm at time levels, $t = 0.0625$, 0.125 and 0.1875 s (numbered as curves 1–6). The arrow annotations, labeled with the curve numbers, point to the corresponding ordinate axis. $\langle \dot{V} \rangle = 16$ ml/min. Instantaneous velocity based on relation $\dot{V}_2$ (Eq. (2)).

stress values are typically half of those in Fig. 19, but the trend in behaviour is the same as in Fig. 19, namely starkly dissimilar $\tau_w$ distributions at $t = 0.0625$ s and $t = 0.1875$ s.

### 3.3. Packed column calculation

Modeling the packed column/bed as a porous zone composed of sources and sink terms in the momentum equations means that as far as the details of the velocity field are concerned, the state of the flow beyond the bed is only of interest. Fig. 21 plots the axial velocity at $Z = 43$ mm along two orthogonal lines at various times, and in comparison to the open column calculation (Fig. 18) there is little difference. In fact, the profiles for the open column calculation are slightly flatter. Comparison of the predicted $\tau_w$ distributions for the open column (Fig. 19) and packed column calculations (not shown for reasons of conciseness) indicate virtually no fundamental differences in behaviour both in terms of trend and magnitudes. The implication of this result for a dosage form located in the tablet holder is that it essentially 'sees' very similar fluid dynamic conditions in both the packed column and open column configurations.

Analogous to the predictions in the open column configuration at $t = 0.1875$ s, $\tau_w$ is markedly different to its counterpart at $t = 0.0625$ s. Upon closer inspection of the velocity field in the immediate vicinity of the tablet, as depicted in Figs. 22 and 23, flow reversal is taking place in the boundary layer surrounding the tablet. The flow in the free-stream is necessarily directed in the positive $Z$-direction, but in the region adjacent to the tablet, the fluid is moving in the negative $Z$-direction. A similar effect can be predicted for the flow in the near-wall region of the ⌀22.6 mm test vessel. This is not apparent from Figs. 18 and 21, where $V_Z = 0$ at $X/Y = \pm 11.3$ mm when $t = 0.1875$ s, but subsequent calculations with a more refined mesh at these near-wall locations confirm flow-reversal there too. Flow reversal, or separation, in a velocity boundary layer is quite common when the fluid is moving against an adverse pressure gra-

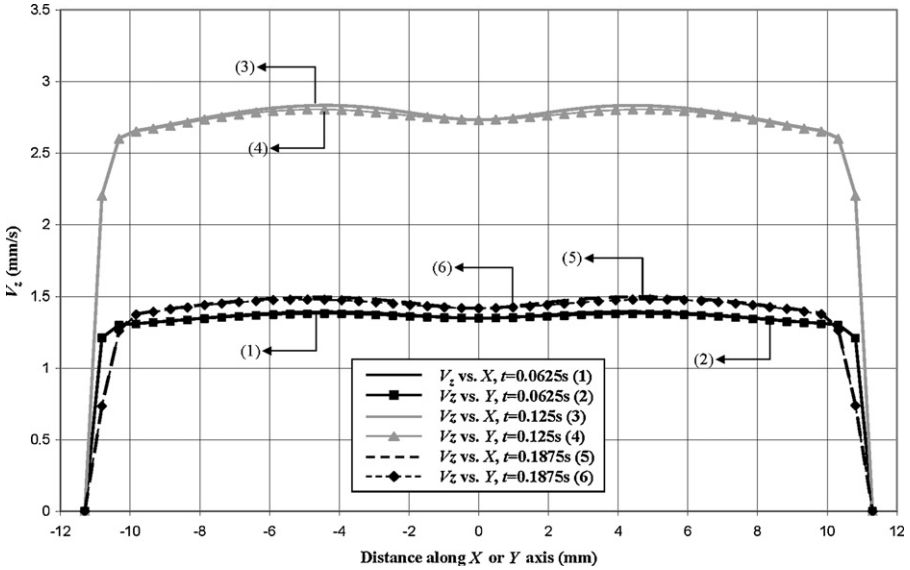


**Fig. 18.** Open column calculation. Axial ($Z$-component) velocity profiles along the line $X = 0$ and $Y = 0$ at $Z = 43$ mm at time levels, $t = 0.0625$, 0.125 and 0.1875 s (numbered as curves 1–6). $\langle \dot{V} \rangle = 16$ ml/min. Instantaneous velocity based on relation $\dot{V}_2$ (Eq. (2)).

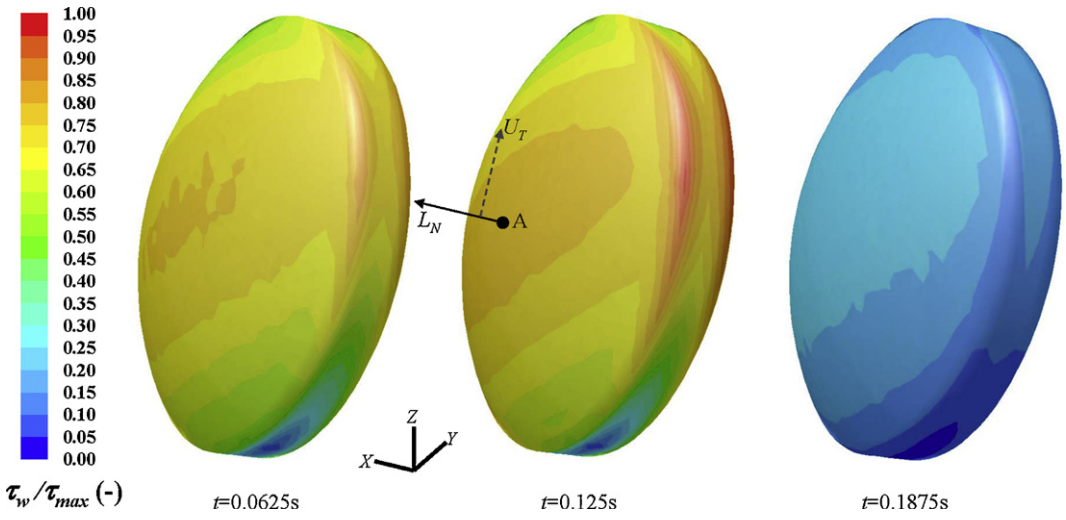


**Fig. 19.** Open column calculation. Contour plot of tablet shear stress, $\tau_w$, normalized with $\tau_{max}$ = 0.011 Pa. Point A, $L_N$ and $U_T$ are defined in Fig. 5. $\langle \dot{V} \rangle$ = 16 ml/min. Instantaneous velocity based on relation $\dot{V}_2$ (Eq. (2)).

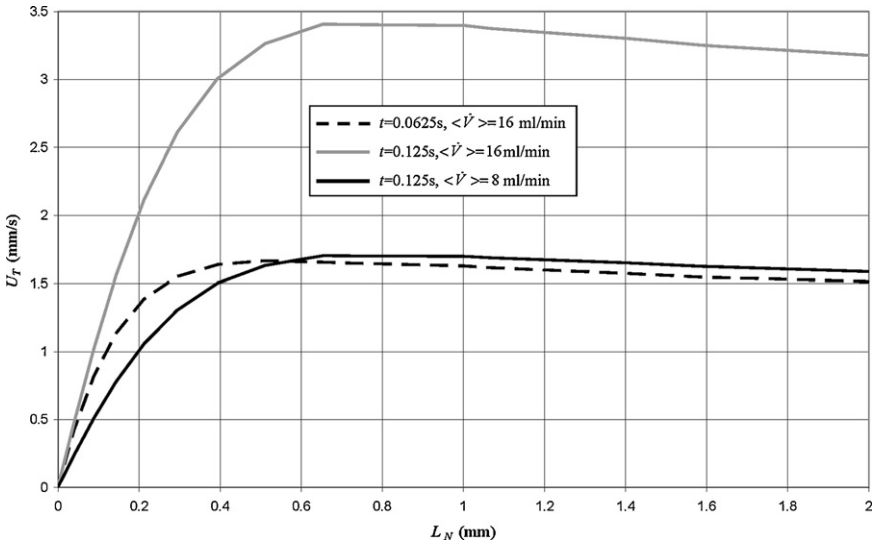


**Fig. 20.** Open column calculation. Profiles of tangential velocity against wall-normal distance relative to point A defined on the tablet surface (Fig. 19). Instantaneous velocity based on relation $\dot{V}_2$ (Eq. (2)).

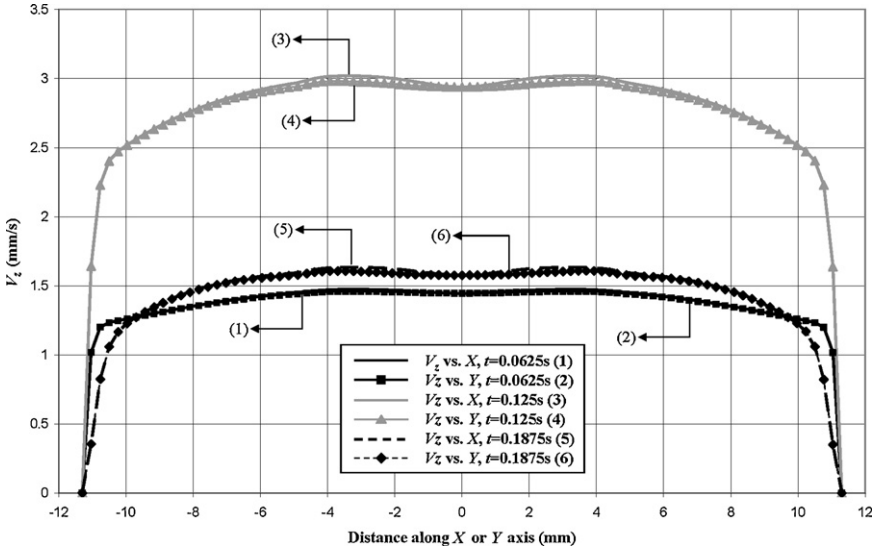


**Fig. 21.** Packed column calculation. Axial ($Z$-component) velocity profiles along the line $X$ = 0 and $Y$ = 0 at $Z$ = 43 mm at time levels, $t$ = 0.0625, 0.125 and 0.1875 s (numbered as curves 1–6). $\langle \dot{V} \rangle$ = 16 ml/min. Instantaneous velocity based on relation $\dot{V}_2$ (Eq. (2)).

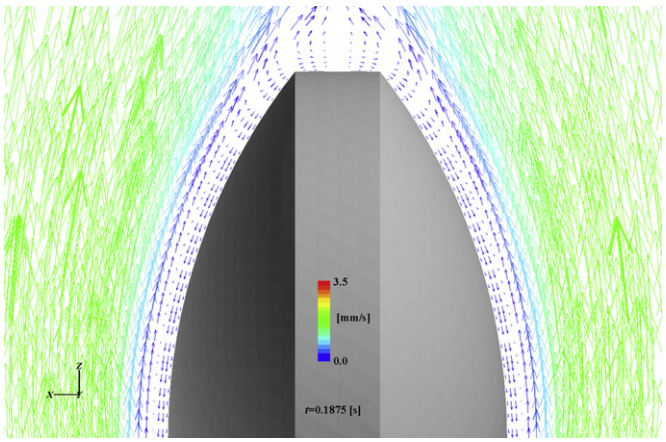


**Fig. 22.** Packed column calculation. Vector plot of $Z$–$X$ component of velocity along plane $Y = 0$ showing top half of tablet at $t = 0.1875$ s. Color legend represents the magnitude of $Z$–$X$ velocity vector. $\langle \dot{V} \rangle = 16$ ml/min. Instantaneous velocity based on relation $\dot{V}_2$ (Eq. (2)).

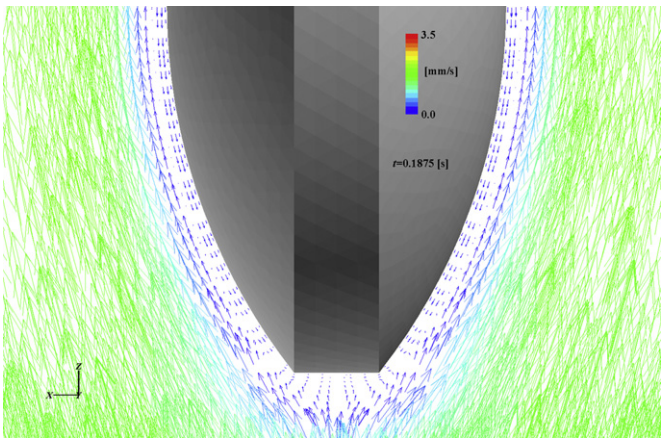


**Fig. 23.** Packed column calculation. Vector plot of $Z$–$X$ component of velocity along plane $Y = 0$ showing bottom half of tablet at $t = 0.1875$ s. Color legend represents the magnitude of $Z$–$X$ velocity vector. $\langle \dot{V} \rangle = 16$ ml/min. Instantaneous velocity based on relation $\dot{V}_2$ (Eq. (2)).

dient (Prandtl, 2001). As a result of a pressure drop in the flow direction, the flow will maintain its direction along the contour of the wall. Should the pressure gradient reverse in the main flow direction, the free-stream flow will be decelerated. Consequently the slower-moving fluid mass in the boundary layer is retarded even further. If the resulting retardation is large enough, the flow will separate from the wall and a recirculation region will appear. As a result of the near-wall reversed flow, the boundary layer thickness grows rapidly, as more fluid mass moves out of the boundary layer

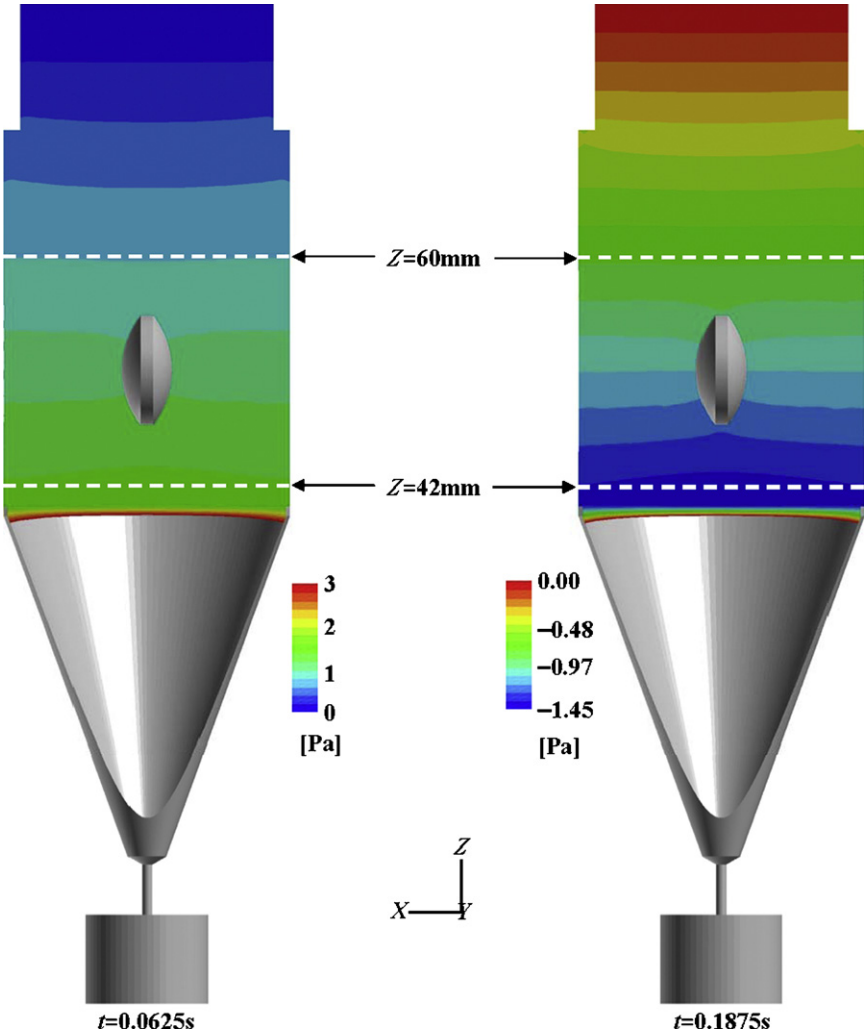


**Fig. 24.** Packed column calculation. Contours of gauge pressure along the plane $Y = 0$ at $t = 0.0625$ s and $t = 0.1875$ s with thresholding of the contour limits to emphasize region of interest. $\langle \dot{V} \rangle = 16$ ml/min. Instantaneous velocity based on relation $\dot{V}_2$ (Eq. (2)).

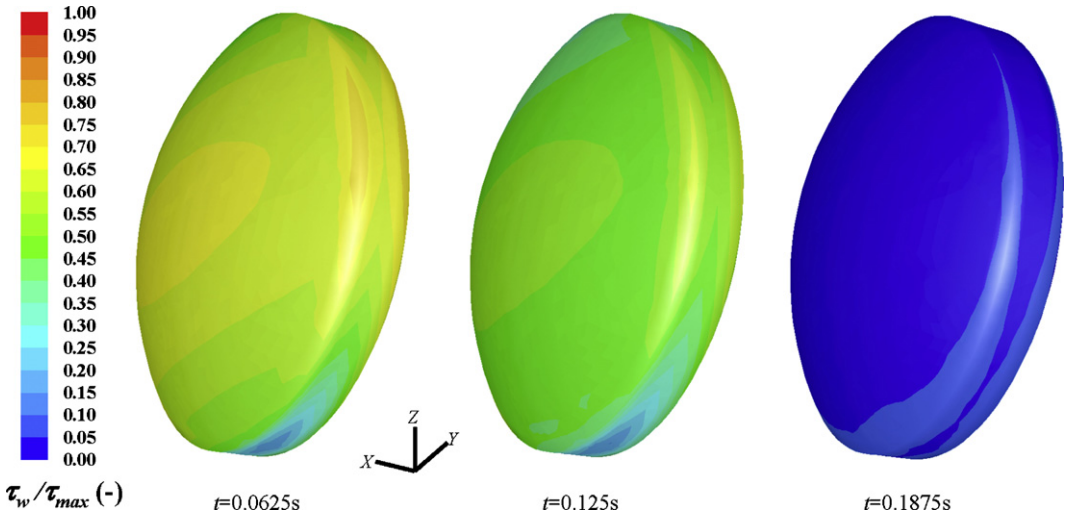


**Fig. 25.** Packed column calculation. Contour plot of tablet shear stress, $\tau_w$, normalized with $\tau_{max} = 0.011$ Pa. $\langle \dot{V} \rangle = 16$ ml/min. Instantaneous velocity based on relation $\dot{V}_1$ (Eq. (1)).

into the free-stream. At the separation point the wall shear stress locally vanishes, or becomes zero. The line of zero velocity dividing the forward and reverse flow leaves the surface at the separation point, and is known as the separation streamline (Massey, 1987). Fig. 24 shows contours of gauge pressure; this is pressure expressed relative to atmospheric/ambient pressure. Analysis of the pressure contours confirms that at $t = 0.1875$ s the gauge pressure just after the packed bed region drops to zero, falls below atmospheric over a short length and then slowly recovers back to the zero Pascal value set as a boundary condition at the outlet to the geometry. In other words as the flow moves up past the tablet it experiences a pressure gradient directed in the negative $Z$-direction. At $t = 0.0625$ s, the situation is the opposite, namely a favorable pressure gradient.

All the results shown thus far have involved the use of the instantaneous velocity profile designated as $\dot{V}_2$, as given by Eq. (2). The alternative profile, $\dot{V}_1$ (Eq. (1)), matches the pump's specification and it is important to verify if the same qualitative features are predicted. Fig. 25 shows $\tau_w$ when the flow is pulsed according to the specification $\dot{V}_1$. At the start of this section it was stated that the $\tau_w$ distributions for the open and packed column calculations pulsed with $\dot{V}_2$ are very similar. Consequently Fig. 25 is compared with Fig. 19, the latter assuming the role of a representative surrogate of the packed column behaviour pulsed with $\dot{V}_2$. Compared to Fig. 19 the results at $t = 0.0625$ s are generally similar. At $t = 0.1875$ s, Fig. 25 indicates near-zero shear stress on a large area of the tablet, whereas Fig. 19 predicts slightly higher values at this time. In contrast, at $t = 0.125$ s in Fig. 25, an overall drop in $\tau_w$ is predicted compared to $t = 0.0625$ s, while it was observed earlier in connection with Fig. 19 (i.e. profile $\dot{V}_2$) that there was little visible change between the $\tau_w$ contours at $t = 0.0625$ s and $t = 0.125$ s. To understand these results, the tablet (near-wall) velocity gradients need to be considered. Fig. 26 confirms the similarity of the $\tau_w$ distributions at $t = 0.0625$ s for profiles $\dot{V}_1$ and $\dot{V}_2$ since the velocity profiles near $L_N = 0$ are quite similar. But at $t = 0.125$ s profile $\dot{V}_2$ gives rise to a steeper velocity profile compared to $\dot{V}_1$, thereby yielding larger $\tau_w$ values. At $t = 0.1875$ s the results demonstrate that there is no flow separation according to $\dot{V}_1$, whereas $\dot{V}_2$ dips below zero. In fact the profile of the curve pertaining to $\dot{V}_1$ at $t = 0.1875$ s is virtually at the point of inflexion, suggesting that flow reversal is imminent.

A complementary result is provided by Fig. 27 which plots the pressure difference ($\Delta P$) transients for both the open and the

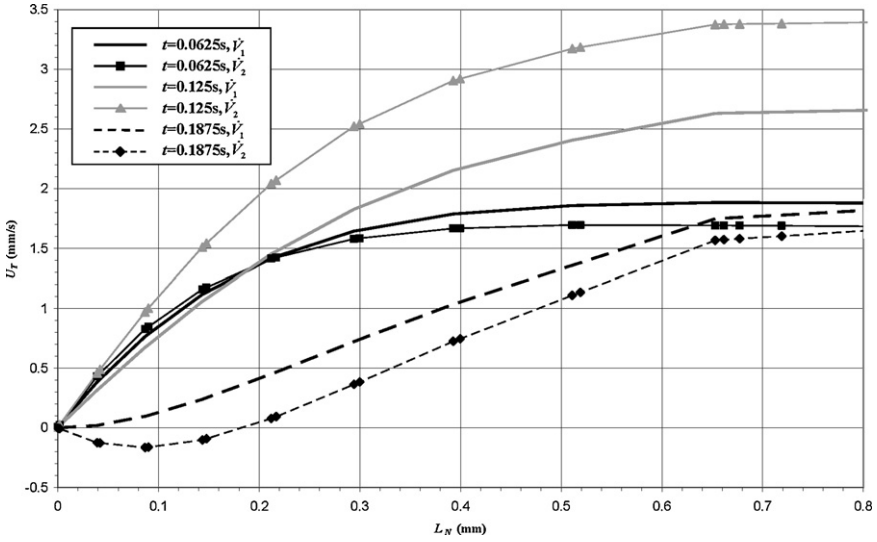


**Fig. 26.** Packed column calculation. Profiles of tangential velocity against wall-normal distance relative to point A defined on the tablet surface (Fig. 19) as a function of the proposed sinusoidal velocity profiles (Eqs. (1) and (2)).

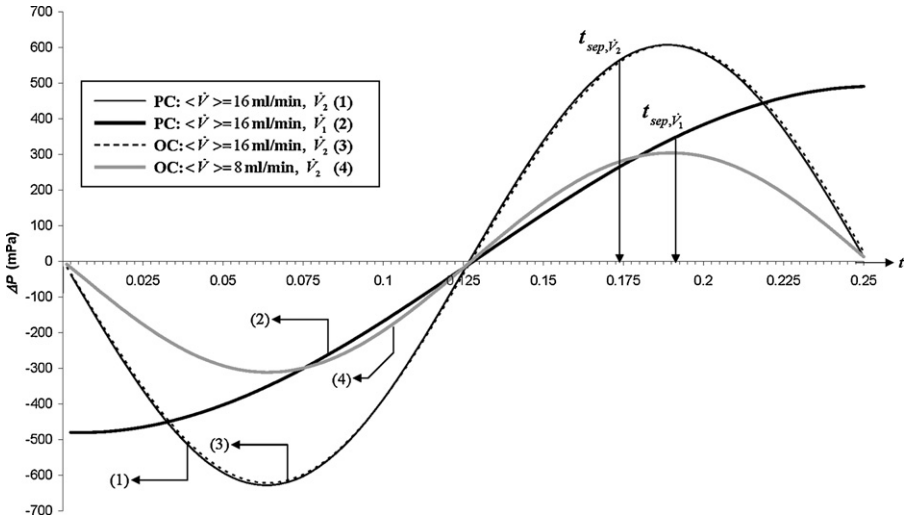


**Fig. 27.** Pressure difference transients across the planes $Z = 60$ mm and $Z = 42$ mm ($\Delta P = P_{Z=60\text{mm}} - P_{Z=42\text{mm}}$) for open column and packed column calculations (numbered as curves 1–4). 'PC' and 'OC' denote packed column and open column respectively.

packed column calculations. This is the pressure difference between planes $Z = 60$ mm and $Z = 42$ mm shown in Fig. 24. Fig. 27 indicates that after the inlet velocity pulse passes its peak value at $t = 0.125$ s, the adverse pressure gradient builds up for both inlet profiles $\dot{V}_1$, and $\dot{V}_2$, in other words $\Delta P > 0$. The difference in wavelength between the pressure transients based on $\dot{V}_1$, and $\dot{V}_2$ follows directly from their respective definitions in Eqs. (1) and (2). The physical explanation for this observation is that $\dot{V}_2$ drops to zero gradually whereas $\dot{V}_1$ has a non-zero gradient at $t = 0$ and $t = 0.25$ s (Fig. 6). At some critical value of $\Delta P$, the competing influences of the inertial and pressure gradient terms in the momentum equation balance out such that the flow is on the verge of separation within the boundary layer regions. For profile $\dot{V}_1$ this occurs for $0.19 < t < 0.1925$ s, and for profile $\dot{V}_2$ in the range $0.1725 < t < 0.175$ s. The precise times are labeled as $t_{sep,\dot{V}_1}$ and $t_{sep,\dot{V}_2}$ in Fig. 27. This explains why at $t = 0.1875$s (in Fig. 26) separation of the boundary layer at the tablet surface was predicted for $\dot{V}_2$ but not $\dot{V}_1$. Depending on the inlet flow profile the same qualitative features are simply shifted in time. The similarity of the pressure transients for the open column and packed column test cases at $\langle \dot{V} \rangle = 16$ ml/min is in agreement with the observation that the predictions in the dissolution test section show little discrepancy. Halving the volumetric flow rate to $\langle \dot{V} \rangle = 8$ ml/min brings about a directly proportional reduction in the pressure difference, as predicted by the Hagen–Poiseuille law for laminar flow. Calculations performed with a *steady, constant* inlet flow rate of 16 ml/min did not manifest any flow reversal effects in the velocity boundary layer. Therefore, the onset of the adverse pressure gradient is a direct consequence of the pulsating nature of the flow.

## 4. Conclusions

The mathematical modeling of the fluid dynamics in the flow-through cell using CFD has provided a number of interesting insights into the details of the hydrodynamic interactions taking place in this apparatus. In the simulation without any beads to equalize the effect of the jet issuing from the ∅0.8 mm bore (the so-called 'no-beads' configuration), a highly inhomogeneous flow field propagates through the column and creates a very localized erosion of the tablet, quantified in terms of the wall shear stress, $\tau_w$. The $\tau_w$ values near the stagnation point of the jet impinging on the tablet exceed those in the open and packed column modes by at least three orders of magnitude. This mode of operation is quite remote from the ideal hydrodynamic conditions which are asserted to prevail in this apparatus.

In the open column configuration very non-uniform, asymmetric flow fields are predicted in the downstream proximity of the red ruby bead during the latter half of the discharge pulse. Furthermore, at nominally similar inlet flow rates (for example at $t = 0.0625$ s and $t = 0.1875$ s), the flow structures in this region differ substantially. This is attributed in part to the interaction of the flow with the direction of movement of the red ruby bead. However, further downstream in the dissolution test section the aforementioned differences arising from the complex, non-linear interactions of the bead movement and the flow disappear almost entirely. At this level of the apparatus, the velocity profile over a significant portion of the cross-section is both flat and symmetrical. Nevertheless, in spite of the very similar approach flow velocity profiles in the dissolution test section at $t = 0.0625$ s and $t = 0.1875$ s, the corresponding $\tau_w$ distributions over the tablet differ markedly. In contrast, very similar $\tau_w$ distributions were predicted at $t = 0.0625$ s and at the pulse's peak ($t = 0.125$ s). The latter result is attributed to the change in boundary layer thickness over the tablet in going from $t = 0.0625$ s to $t = 0.125$ s. As would be expected intuitively, a halving of the average flow rate leads to a proportional reduction in the predicted $\tau_w$ distribution. A preliminary conclusion therefore appears to be that the degree of shearing erosion the tablet experiences correlates with the average flow rate; however during the phase of a particular pulse both the free-stream velocity of approach *and* the growth of the boundary layer need to be taken into consideration.

The aforementioned effects in the open column calculations are also observed in the packed column calculations at the level of the dissolution test section as evidenced by the similarity and symmetry of the velocity profiles. This lends support to the notion that the flow in this region of the apparatus is indeed very uniform. However, this does not necessarily imply that two real tablets from the same batch would dissolve at the same rate if tested under open and packed column configurations. Rather, the predictions suggest that if differences in drug release rates are observed experimentally, they should not be attributable to variability in fluid dynamic effects. It can even be argued that the tablet is subjected to the same flow in both open and packed column modes provided it remains in the tablet holder. This condition is satisfied during the initial phases of dissolution when appreciable loss of surface area or disintegration has not occurred.

The disparity in the $\tau_w$ distributions on the tablet surface at $t = 0.0625$ s and $t = 0.1875$ s is associated with flow reversal in the velocity boundary layer at the latter time resulting from an overall adverse pressure gradient in the vicinity of the tablet during the downswing of the discharge pulse. The separation of the velocity boundary occurs over most of the length of the tablet and the bounding dissolution vessel wall. This effect is not predicted when the inlet velocity profile is held at a constant value (i.e. with non-pulsating flow). The effect of changing the instantaneous inlet sinusoidal profile on the prediction of flow separation, while maintaining the same average flow rate, is to modulate the precise time at which this phenomenon is observed. Higher $\tau_w$ values are predicted for the profile which generates a higher local peak velocity, which reinforces the idea that for correct calibration not only the average, but also the instantaneous profile may require more precise characterization than what is currently detailed in the compendia.

Important assumptions and simplifications associated with this modeling work relate to the explicitly prescribed bead movement and the specification of a constant zero gauge pressure at the defined outlet to the model geometry during the entire pump discharge stroke. Experimental verification is clearly required to help assess the validity of the assumptions made in this work, and more generally the aforementioned observations based on the predictions.

## Appendix A. Nomenclature

| | |
|---|---|
| $C$ | inertial loss resistance in porous zone formulation ($m^{-1}$) |
| $d_{eff}$ | effective particle diameter defined as $d_{eff} = 6/S_V$ where $S_V$ is the surface to volume ratio over all the particles (m) |
| $d_{\varnothing 1mm}$ | diameter of 1 mm glass bead (m) |
| $f$ | friction factor, defined as $f = (\Delta P/h)(d_{eff}/\rho U_s^2)[\varepsilon^3/(1-\varepsilon)]$ |
| $h$ | height of packed column of uniform cross-section (m) |
| $L_N$ | wall-normal distance above point A defined on tablet surface, as illustrated in Fig. 5 (m) |
| $L_p$ | displacement of red ruby bead relative to its rest state (m) |
| $L_{p,max}$ | (maximum) lift of red ruby bead relative to its rest state (m) |
| $N_s$ | number of cycles of pump per second ($s^{-1}$) |
| $Re'$ | modified Reynolds number defined as $Re' = \rho U_s d_{eff}/\mu(1-\varepsilon)$ |
| $S_i$ | source term in momentum equation for porous zone formulation in direction $i$ ($i = 1$–3 corresponds to $X$, $Y$, $Z$ respectively in Cartesian space) (Pa $m^{-1}$) |
| $t$ | time (s, min) |
| $t_{sep,\dot{V}_1}$ | time to flow separation in tablet velocity boundary layer pulsed with $\dot{V}_1$ (s) |
| $t_{sep,\dot{V}_2}$ | time to flow separation in tablet velocity boundary layer pulsed with $\dot{V}_2$ (s) |
| $U_p$ | velocity of red ruby bead ($ms^{-1}$) |
| $U_s$ | superficial velocity through the ∅1 mm glass bead packing in the mean flow direction ($ms^{-1}$) |
| $U_T$ | velocity component orthogonally oriented to $L_N$ above point A, as defined in Fig. 5 ($ms^{-1}$) |
| $u_i$ | physical velocity through the ∅1 mm glass bead packing in direction $i$ ($i = 1$–3 corresponds to $X$, $Y$, $Z$ respectively in Cartesian space), defined as $u_i = U_s/\varepsilon$ ($ms^{-1}$) |
| $V_{Bed}$ | volume occupied by random packing (including empty space of interstices) of ∅1 mm glass bead in the dissolution vessel ($m^3$) |
| $V_{max}$ | volume of fluid dispensed in cell at a given average flow rate during the discharge stroke of pump defined as $V_{max} = \langle\dot{V}\rangle/N_s$ ($m^3$) |
| $V_{Solid}$ | solid volume occupied by ∅1 mm glass bead in the dissolution vessel ($m^3$) |
| $\dot{V}_1$ | instantaneous volumetric flow (or discharge) rate based on Eq. (1) (ml/min, $m^3\ s^{-1}$) |
| $\dot{V}_2$ | instantaneous volumetric flow (or discharge) rate based on Eq. (2) (ml/min, $m^3\ s^{-1}$) |
| $\langle\dot{V}\rangle$ | average volumetric flow (or discharge) rate (ml/min, $m^3\ s^{-1}$) |
| $\dot{V}_{1,max}$ | peak discharge rate in cell based on profile 1 (Eq. (1)) and given by $\dot{V}_{1,max} = \pi N_s V_{max}$ (ml/min, $m^3\ s^{-1}$) |
| $\dot{V}_{2,max}$ | peak discharge rate in cell based on profile 2 (Eq. (2)) and given by $\dot{V}_{2,max} = 4N_s V_{max}$ (ml/min, $m^3\ s^{-1}$) |
| $V_z$ | axial ($Z$-)component of velocity vector ($ms^{-1}$) |

*Greek letters*

| | |
|---|---|
| $\alpha$ | permeability of porous zone ($m^2$) |
| $\Delta P$ | pressure difference (or pressure drop in definition of friction factor) (Pa) |
| $\varepsilon$ | voidage fraction in packed column |
| $\mu$ | dynamic (absolute) viscosity of fluid/dissolution medium (Pa s) |
| $\rho$ | density of fluid/dissolution medium ($kg\ m^{-3}$) |
| $\rho_{bulk}$ | bulk density of ∅1 mm glass beads ($kg\ m^{-3}$) |
| $\rho_{Solid}$ | material density of ∅1 mm glass beads ($kg\ m^{-3}$) |
| $\tau_w$ | tablet shear stress (Pa) |
| $\tau_{max}$ | maximum tablet shear stress from open and closed column calculations (Pa) |
| ∅ | prefix used to denote diameter, e.g. ∅0.8 mm denotes cross-section of column where local diameter is 0.8 mm. |

## Disclaimer

The views expressed in this paper are those of the author and do not reflect the opinion nor the policy of the FDA.

## References


Ansys Inc., 2008. 10 Cavendish Court, Lebanon NH 03766 USA. www.fluent.us.

Bai, G.E., Armenante, P.M., Plank, R.V., Gentzler, M., Ford, K., Harmon, P., 2007a. Hydrodynamic investigation of USP dissolution test apparatus II. J. Pharm. Sci. 96, 2327–2349.

Bai, G.E., Armenante, P.M., Plank, R.V., 2007b. Experimental and computational determination of blend time in USP dissolution testing apparatus II. J. Pharm. Sci. 96, 3072–3086.

Bai, G.E., Armenante, P.M., 2008. Hydrodynamic, mass transfer, and dissolution effects induced by tablet location during dissolution testing. J. Pharm. Sci. 98, 1511–1531.

Baxter, J.L., Kukura, J., Muzzio, F.J., 2005. Hydrodynamics-induced variability in the USP apparatus II dissolution test. Int. J. Pharm. 292, 17–28.

Bhattachar, S.N., Wesley, J.A., Fioritto, A., Martin, P.J., Babu, S.R., 2002. Dissolution testing of a poorly soluble compound using the flow-through dissolution apparatus. Int. J. Pharm. 236, 135–143.

Bird, R.B., Stewart, W.E., Lightfoot, E.N., 1960. Transport Phenomena. John Wiley & Sons, Inc.

Bocanegra, L.M., Morris, G.J., Jurewicz, J.T., Mauger, J.W., 1990. Fluid and particle laser doppler velocity measurements and mass transfer predictions for the USP paddle method dissolution apparatus. Drug Dev. Ind. Pharm. 16, 1441–1464.

Bradshaw, P., 1971. An Introduction to Turbulence and its Measurement. Pergamon Press.

Cammarn, S.R., Sakr, A., 2000. Predicting dissolution via hydrodynamics: salicylic acid tablets in flow through cell dissolution. Int. J. Pharm. 201, 199–209.

D'Arcy, D., Corrigan, O., Healy, A.M., 2005. Hydrodynamic simulation (computational fluid dynamics) of asymmetrically positioned tablets in the paddle dissolution apparatus: impact on dissolution rate and variability. J. Pharm. Pharmacol. 57, 1243–1250.

D'Arcy, D.M., Corrigan, O.I., Healy, A.M., 2006. Evaluation of hydrodynamics in the basket dissolution apparatus using computational fluid dynamics—dissolution rate implications. Eur. J. Pharm. Sci. 27, 259–267.

Ergun, S., 1952. Fluid flow through packed columns. Chem. Eng. Prog. 48, 89–94.

FIP, 1981. Guidelines for dissolution testing of solid oral products. Pharm. Ind. 43, 334–343.

Fluent 6.3 User's Guide, 2006 (Chapter 7: 19 Porous Media Conditions). Ansys Inc. 10 Cavendish Court, Lebanon, NH 03766, USA.

Gao, Z., 2006. Private communication. FDA, Center for Drug Evaluation and Research, Division of Pharmaceutical Analysis, St. Louis, MO 63101, USA.
Gao, Z., Moore, T.W., Smith, A.P., Doub, W.H., Westenberger, B.J., 2007. Studies of variability in dissolution testing with USP apparatus 2. J. Pharm. Sci. 96, 1794–1801.
Hamlin, W.E., Nelson, E., Ballard, B.E., Wagner, J.G., 1962. Loss of sensitivity in distinguishing real differences in dissolution rates due to increased intensity of agitation. J. Pharm. Sci. 51, 432–435.
Howard, J.R., 1989. Fluidized Bed Technology, Principles and Applications. Adam Hilger.
Hu, X., 2007. Private communication. Ansys Inc. 3005 Boardwalk Suite 100, Ann Arbor, MI 48108, USA.
Kakhi, M., 2009. Classification of the flow regimes in the flow-through cell. Eur. J. Pharm. Sci., doi:10.1016/j.ejps.2009.04.003, in press.
Kukura, J., Arratia, P.E., Szalai, E.S., Muzzio, F.J., 2003. Engineering tools for understanding the hydrodynamics of dissolution tests. Drug Dev. Ind. Pharm. 29, 231–239.
Kukura, J., Baxter, J.L., Muzzio, F.J., 2004. Shear distribution and variability in the USP Apparatus 2 under turbulent conditions. Int. J. Pharm. 279, 9–17.
Kunii, D., Levenspiel, O., 1991. Fluidization Engineering, second ed. Butterworth-Heinemann.
Langenbucher, F., Benz, D., Kürth, W., Möller, H., Otz, M., 1989. Standardized flow-cell method as an alternative to existing pharmacopoeial dissolution testing. Pharm. Ind. 51, 1276–1281.
Magnier, M., 2008. Private communication. Sotax AG, Binningerstrasse 106, CH-4123 Allschwil, Switzerland.
Massey, B.S., 1987. Mechanics of Fluids, fifth ed. Van Nostrand Reinhold, UK.
McCarthy, L.G., Kosiol, C., Healy, A.M., Bradley, G., Sexton, J.C., Corrigan, O.I., 2003. Simulating the hydrodynamic conditions in the United States pharmacopeia paddle dissolution apparatus. AAPS PharmSciTech 4 (Article 22).
McCarthy, L.G., Bradley, G., Sexton, J.C., Corrigan, O.I., Healy, A.M., 2004. Computational fluid dynamics modeling of the paddle dissolution apparatus: agitation rate, mixing patterns, and fluid velocities. AAPS PharmSciTech 5, Article 31.
Möller, H., 1983. Dissolution testing of different dosage forms using the flow-through method. Pharm. Ind. 45, 617–622.
Patankar, S.V., 1980. Numerical Heat Transfer and Fluid Flow. Hemisphere Publishing Corp.
Prandtl, L., 2001. In: Oertel, H., (Ed.), Prandtl-Führer durch die Strömungslehre, 10th ed., Fiedr. Vieweg & Sohn Verlagsgesellschaft mbH, Braunschweig/Wiesbaden.
Sandoz Fils SA, 2008. Chemin du Saugy, CH-1482 Cugy, Switzerland. Technical Characteristics of Synthetic Ruby Verneuil Crystals. http://www.sandoz.ch/2002/products/ruby.php.
Schwartz, C.E., Smith, J.M., 1953. Flow Distribution in Packed Beds. Ind. Eng. Chem. 45, 1209–1218.
Sigmund Lindner GmbH, 2008. Oberwarmensteinacher Strasse 38, 95485 Warmensteinach, Germany. Type P - Soda Lime Glass Beads (SiLibeads®). http://www.sigmund-lindner.com.
Tatterson, G.B., 1991. Fluid Mixing and Gas Dispersion in Agitated Tanks. McGraw-Hill.
Tingstad, J.E., Riegelman, S., 1970. Dissolution rate studies I: design and evaluation of a continuous flow apparatus. J. Pharm. Sci. 59, 692–696.
United States Pharmacopeia 31/National Formulary 26. 2008. General Chapter <711> Dissolution. 12601 Twinbrook Parkway, Rockville, Maryland 20852-1790, USA.
VDI Wärmeatlas, 1991. sixth ed. VDI-Verlag GmbH, Düsseldorf.
Wendt, J.F. (Ed.), 1996. Computational Fluid Dynamics, An Introduction, second ed. Springer.
Wennergren, B., Lindberg, J., Nicklasson, M., Nilsson, G., Nyberg, G., Ahlgren, R., Persson, C., Palm, B., 1989. A collaborative in vitro dissolution study: comparing the flow-through method with the USP paddle method using USP prednisone calibrator tablets. Int. J. Pharm. 53, 35–41.
White, F.M., 1994. Fluid Mechanics, third ed. McGraw-Hill.
Wilcox, D.C., 2004. Turbulence Modeling for CFD, second ed. DCW Industries Inc, p. 121.